

1 Development of an aerosol chemical transport model RAQM2  
2 and predictions of Northeast Asian aerosol mass, size,  
3 chemistry, and mixing type.

4

5 M. Kajino<sup>1,2</sup>, Y. Inomata<sup>3</sup>, K. Sato<sup>3</sup>, H. Ueda<sup>4</sup>, Z. Han<sup>5</sup>, J. An<sup>5</sup>, G. Katata<sup>6</sup>, M. Deushi<sup>1</sup>,  
6 T. Maki<sup>1</sup>, N. Oshima<sup>1</sup>, J. Kurokawa<sup>3</sup>, T. Ohara<sup>7</sup>, A. Takami<sup>7</sup>, and S. Hatakeyama<sup>8</sup>

7 [1]{Meteorological Research Institute, Japan Meteorological Agency, 1-1 Nagamine,  
8 Tsukuba 305-0052, Japan}

9 [2]{Pacific Northwest National Laboratory, P.O.Box 999 Richland WA 99352, USA}

10 [3]{Asia Center for Air Pollution Research, 1182 Sowa, Nishi, Niigata 950-2144, Japan}

11 [4]{Toyohashi Institute of Technology, 1-1 Hibarigaoka, Tempaku, Toyohashi 950-2144,  
12 Japan}

13 [5] {Institute of Atmospheric Physics, Chinese Academy of Sciences, Beijing 100029, China}

14 [6] {Japan Atomic Energy Agency, 2-4 Shirakata-shirane, Tokai, Ibaraki 319-1195, Japan}

15 [7] {National Institute for Environmental Studies, 16-2 Onogawa, Tsukuba 305-8506, Japan}

16 [8] {Tokyo University of Agriculture and Technology, 3-5-8 Saiwaicho, Fuchu, Tokyo 183-  
17 8509, Japan}

18 Correspondence to: M. Kajino (kajino@mri-jma.go.jp)

19

20 Short title: Development of RAQM2 and Asian aerosol mixing type simulation

21

22

23

24

1 Abstract

2 A new aerosol chemical transport model, Regional Air Quality Model 2 (RAQM2), was  
3 developed to simulate Asian air quality. We implemented a simple version of a triple-moment  
4 modal-moment aerosol dynamics model (MADMS) and achieved a completely dynamic (non-  
5 equilibrium) solution of a gas-to-particle mass transfer over a wide range of aerosol diameters  
6 from 1 nm to super  $\mu\text{m}$ . To consider a variety of atmospheric aerosol properties, a category  
7 approach was utilized, in which the aerosols were distributed into 4 categories: particles in  
8 Aitken mode (ATK), soot-free particles in accumulation mode (ACM), soot aggregates  
9 (AGR), and particles in coarse mode (COR). In the current setting, aerosol size distribution in  
10 each category is characterized by a single mode. Condensation, evaporation, and Brownian  
11 coagulations for each mode were solved dynamically. A regional-scale simulation ( $\Delta x = 60$   
12 km) was performed for the entire year of 2006 covering the Northeast Asian region. Statistical  
13 analyses showed that the model reproduced the regional-scale transport and transformation of  
14 the major inorganic anthropogenic and natural air constituents almost within factors of 2 to 5.  
15 The modeled  $\text{PM}_{10}$ /bulk ratios of the chemical components were consistent with the  
16 observations, indicating that the simulated aerosol mixing types were consistent with those in  
17 nature. Non-sea salt  $\text{SO}_4^{2-}$  mixed with ATK + ACM was the largest at Hedo in summer,  
18 whereas it mixed with AGR was substantial in cold seasons. Ninety-eight percent of the  
19 modeled  $\text{NO}_3^-$  was mixed with sea salt at Hedo, whereas 53.7% of the  $\text{NO}_3^-$  was mixed with  
20 sea salt at Gosan, located upwind toward the Asian continent. The condensation of  $\text{HNO}_3$   
21 onto sea salt particles during transport over the ocean makes the difference in the  $\text{NO}_3^-$  mixing  
22 type at the two sites. Because the aerosol mixing type alters optical properties and cloud  
23 condensation nuclei activity, its accurate prediction and evaluation are indispensable for  
24 aerosol-cloud-radiation interaction studies.

25

26 **Keywords:** air quality modeling, aerosol category approach, non-equilibrium aerosol  
27 dynamics, Northeast Asia

28

29

30

31

1

## 2 1 Introduction

3 Atmospheric trace gases and aerosols have various detrimental effects on ecosystems and  
4 human health. Because their emission, secondary formation, transport and deposition  
5 mechanisms are highly complex and still unknown, a great number of studies on the  
6 development and application of air quality modeling are ongoing. Recently, Jacobson and  
7 Ginnebaugh (2010) developed a global-through-urban nested three-dimensional air pollution  
8 model that implements a large explicit photochemical mechanism with 4,675 gases and  
9 13,626 tropospheric and stratospheric chemical reactions. The mechanism also includes one  
10 internally mixed aerosol and three hydrometeor categories that are size and chemistry  
11 resolved (17 components  $\times$  14 size bins for aerosols, 18 components  $\times$  30 size bins for  
12 cloud/precipitation liquid, cloud/precipitation ice, cloud/precipitation graupel). On the other  
13 hand, there is still a high demand for computationally efficient models for the purpose of  
14 long-term integration with higher grid resolutions. For example, the Community Multiscale  
15 Air Quality (CMAQ) model (Byun and Schere, 2006) was extensively used worldwide and  
16 was continually updated for more than 10 years to the current version 4.7 (Foley et al., 2010).

17 Asian air quality is highly complex because it covers the tropics to the polar zones with  
18 huge amounts of anthropogenic air pollutants and natural Asian dust particles together with  
19 other natural species. The Regional Air Quality Model (RAQM) was developed at the Acid  
20 Deposition and Oxidant Research Center (currently changed to the Asia Center for Air  
21 Pollution Research), which focuses on such Asian air quality problems (An et al., 2002; Han,  
22 2007). The model has been used for various air pollution studies in Asia, such as studies on  
23 high oxidant, massive dust transport, and volcanic sulfur episodes, and substantial  
24 modifications have been made based on comparison and evaluation with extensive and long-  
25 term monitoring data (An et al., 2002, 2003; Han, 2007; Han et al., 2004, 2005, 2006; Kajino  
26 et al., 2004, 2005) and with other models (Carmichael et al., 2008 and references therein).  
27 However, an aerosol dynamics module was not implemented in RAQM, and thermodynamic  
28 equilibrium was assumed for the gas-aerosol partitioning of semi-volatile inorganic  
29 components such as sulfate, nitrate and ammonium.

30 To simulate the evolutionary processes of aerosol microscale properties such as chemical  
31 compositions, size distribution and mixing state, we implemented a simple version of a new  
32 modal-moment aerosol dynamics model (Kajino, 2011; Kajino and Kondo, 2011) that enables

1 the non-equilibrium calculation of gas-to-particle mass transfer over a wide range of aerosol  
2 diameters from 1 nm to super-micrometer particles. We also implemented six important  
3 parameterizations relating to aerosol dynamics: 1. new particle formation, 2. cloud  
4 condensation nuclei (CCN) activation, 3. ice nuclei (IN) activation, 4. an explicit grid-scale  
5 cloud microphysical module, 5. dry deposition, and 6. sub-grid-scale convection and  
6 scavenging.

7 The new model is referred to as RAQM2. In Sect. 2, a unique aerosol dynamics module is  
8 described in detail together with the above parameterizations. The model results are evaluated  
9 in Sect. 3 using the Acid Deposition Monitoring Network in East Asia (EANET) and the Cape  
10 Hedo Atmosphere and Aerosol Monitoring Station (CHAAMS). The major findings are  
11 summarized in Sect. 4.

12

## 13 2 Model description

### 14 2.1 General description of the WRF/RAQM2 framework and parameterizations 15 used in the models

16 In this section, a general description of an offline-coupled meteorology – chemical transport  
17 framework (WRFV3/RAQM2) is presented; however, because the aerosol dynamics model of  
18 RAQM2 is unique, it is described in detail in Sect. 2.2. Table 1 summarizes the list of data  
19 and schemes used in the WRF and RAQM2 models.

20 Fig. 1 illustrates the model domain of WRF and RAQM2, and the locations of the observation  
21 sites of the Acid Deposition Monitoring Network in East Asia (EANET) and the Cape Hedo  
22 Atmosphere and Aerosol Monitoring Station (CHAAMS). There are horizontally  $90 \times 60$  grids  
23 with 60km grid resolution on a Lambert conformal map projection. There are vertically 28  
24 layers from the ground to 100 hPa for WRF and 13 layers to 10 km for RAQM2 with terrain-  
25 following coordinates. The horizontal grid points are common to both WRF and RAQM2,  
26 whereas the vertical grid points are different. After the spline vertical interpolation of wind  
27 velocity and air density to the RAQM2 levels, the mass balance is not maintained. Thus, the  
28 mass continuity model MSCWM (Ishikawa, 1994) is used to reduce the mass divergence due  
29 to the vertical interpolation to about  $10^{-5}$  to  $10^{-6}$  ( $s^{-1}$ ). The input/output time interval for WRF-  
30 RAQM2 was set to 1 h. For the lateral and upper boundary concentrations of the RAQM2  
31 simulation, the climatological simulation results of monthly  $NO_x$ ,  $O_x$ , CO and volatile organic

1 compound (VOC) concentrations were used using a global-scale stratospheric and  
2 tropospheric chemistry climate model (MRI-CCM2; Deushi and Shibata, 2011). The entire  
3 simulation period was 1 year, but each simulation was performed separately for each month  
4 (as most of the boundary data sets are on monthly basis), with a spin-up period of 2 weeks for  
5 RAQM2. WRF simulation was done for a year at once with a spin-up period of 3 days.

6 RAQM2 incorporates major processes for atmospheric trace species, such as anthropogenic  
7 and natural emissions, advection, turbulent diffusion, photochemistry, new particle formation,  
8 condensation, evaporation, Brownian coagulation, dry deposition, grid-scale cloud  
9 condensation nuclei (CCN) and ice nuclei (IN) activation and subsequent cloud microphysical  
10 processes, grid-scale aqueous chemistry in hydrometeors as well as in aerosol water, subgrid-  
11 scale convection and wet scavenging (Table 1).

12 The emission inventory was obtained from REAS (Ohara et al., 2007), which was extended to  
13 the year 2005 (Kurokawa et al., 2009). The emitted species are NO<sub>x</sub>, SO<sub>2</sub>, NH<sub>3</sub>, NMVOCs  
14 (Non-Methane Volatile Organic Compounds), BC (Black Carbon), and POAs (Primary  
15 Organic Aerosols). Because REAS does not provide seasonal variations of the emission flux,  
16 we applied the simple monthly variations for Chinese emissions (Table 9 of Zhang et al.,  
17 2009). The temporal variations of the anthropogenic emission flux are not considered in the  
18 current setting. We used the Global Fire Emissions Database (GFED3; Giglio et al., 2010) for  
19 open biomass burning emissions (NO<sub>x</sub>, SO<sub>2</sub>, NMVOCs, BC and, POA) and the Model of  
20 Emissions of Gases and Aerosols from Nature (MEGAN2; Guenther et al., 2006) for biogenic  
21 emissions (isoprene and terpenes). Clarke et al. (2006) was used for sea salt production and  
22 Han et al. (2004) for the dust deflation process. The fractions of crustal elements such as Na<sup>+</sup>,  
23 Ca<sup>2+</sup>, Mg<sup>2+</sup>, and K<sup>+</sup> in sea salt and Asian dust particles are derived from Song and Carmichael  
24 (2001). However, using the above combinations, the PM<sub>10</sub> and non-sea salt (nss) Ca<sup>2+</sup> were  
25 overestimated during the dust transport season in spring 2006 in Japan. There have been  
26 substantial efforts to adjust dust emission flux and transport by developing sophisticated  
27 physical deflation models (Kang et al., 2011, and references therein) or by applying state-of-  
28 the-art data assimilation techniques (e.g., Yumimoto et al., 2008; Sekiyama et al., 2010).  
29 Because deducing the accurate dust emission flux was not a focus of this study, we simply  
30 reduced the dust emission to one quarter uniformly in time and in space and the Ca<sup>2+</sup> contents  
31 (6.8 wt%) in the Asian dust to half (3.4 wt%) to roughly adjust to both the observed PM<sub>10</sub> and  
32 the nss-Ca<sup>2+</sup> concentration at the Japan EANET stations for 2006. The value of 3.4 wt% is

1 smaller than that in previous works, such as Song and Carmichael (2001) and Wang et al.  
2 (2002), but the value is still plausible compared with the China-map project data (available at  
3 [http://www.cgrrer.uiowa.edu/EMISSION\\_DATA/biogeo/Ca-chinamap.gif](http://www.cgrrer.uiowa.edu/EMISSION_DATA/biogeo/Ca-chinamap.gif)).

4 The SAPRC99 mechanism (Carter, 2000) was implemented for gas phase photochemistry,  
5 together with additional Secondary Organic Aerosol (SOA) formation mechanism (Edney et  
6 al., 2007). However, because the contribution of SOA mass produced by the model was found  
7 to be less significant to the East Asian regional-scale simulations and because we focused  
8 mainly on the behaviors of inorganic components, the process was not included in the current  
9 study. The aqueous phase chemistry in grid-scale cloud and rain water droplets as well as  
10 aerosol water was considered (Walcek and Taylor, 1986; Carlton et al., 2007). The wet  
11 scavenging due to the subgrid-scale convection was considered using the Asymmetrical  
12 Convective Model (Pleim and Chang, 1992), whereas aqueous phase chemistry in convective  
13 clouds was not considered. Zhang et al. (2003) was used to calculate the dry deposition  
14 velocities of gaseous species. The monthly composite MODIS/LAI data processed from  
15 MOD15A2 (available from <https://lpdaac.usgs.gov/products>; Myneni et al., 2002; Yang et al.,  
16 2006) are used to obtain realistic values for the surface resistances of the dry deposition  
17 velocity. Aerosol dry deposition is calculated using the method of Zhang et al. (2001) with  
18 modifications to improve the prediction accuracy, as described in detail in Sect. 2.2.8.

## 19 2.2 Formulations of a fully dynamic aerosol module

20 The current aerosol module is a three moment bulk dynamics model that conserves number,  
21 surface area, and mass concentrations of aerosol populations under the assumption that sizes  
22 of aerosols can be represented by uni-modal lognormal size distributions (LNSDs). In this  
23 section, an aerosol category approach is introduced that presents dynamical and chemical  
24 evolutions in the mass and size distributions of aerosols due to emissions, new particle  
25 formation, condensation, Brownian coagulation, dry deposition, CCN activation, IN  
26 activation, and cloud microphysical processes using a modal-moment dynamics approach.

### 27 2.2.1 Simple version of a **triple-moment** aerosol module MADMS

28 A simple version of a **triple-moment** aerosol module called Modal Aerosol Dynamics model  
29 for multiple Modes and fractal Shapes (MADMS; Kajino, 2011) was implemented in  
30 RAQM2. MADMS can simulate the Brownian coagulation of a couple of modes with very

1 different LNSD parameters and with different mass fractal dimensions ( $D_f$ ) of aggregates.  
2 Simply, in RAQM2, all the particles were assumed to be spherical ( $D_f=3$ ).

3 As shown in Table 2, the populations of aerosols were grouped into 4 categories: 1. **particles**  
4 **in** Aitken mode (ATK); 2. **soot-free particles in** accumulation mode (ACM); 3. soot  
5 aggregates (AGR); and 4. **particles in** coarse mode (COR). The ATK category represents an  
6 assemblage of aerosols formed by new particle formation and growing through the  
7 coagulation and condensation of trace gases and water vapor. The ACM category includes a  
8 part of the ATK aerosols that evolved to be larger than a certain diameter (set as 40 nm in this  
9 study) as well as organic compounds and unidentified mass, and it excludes BC particles. The  
10 AGR category indicates soot aggregates generated through combustion, and it contains BC  
11 particles. Therefore, the ATK and ACM are non-light-absorbing particles, whereas AGR are  
12 light-absorbing particles. Without separating the AGR category from the others, the evolution  
13 of the mixing state of BC particles cannot be considered, which alters the absorption of solar  
14 radiation and the number of CCN particles. The COR category includes mechanically  
15 produced natural aerosols such as dust and sea salt particles as well as unidentified  
16 components from  $PM_{10}$  emissions.

17 The aerosol sizes in each category were assumed to be characterized by a uni-modal LNSD.  
18 **There are three parameters ~~were used~~ to characterize** the LNSD **function**: the number  
19 concentration  $N$ , the geometric mean diameter  $D_g$ , and the geometric standard deviation  $\sigma_g$ .  
20 **Instead of the three parameters**, in the modal-moment dynamics modeling, the temporal  
21 evolutions of the three moments were solved to **characterize the changes in the** LNSD. The  
22  $k$ th moment is defined as

$$M_k = \int_{-\infty}^{\infty} D^k n(\ln D) d(\ln D) \quad (1)$$

24

Applying the Gaussian integral formula to Eq. (1) results in

25

$$M_k = ND_g^k \exp\left[\frac{k^2}{2} \ln^2 \sigma\right] \quad (2)$$

26 A list of **transported species** of each category is shown in Table 2. The zeroth and second  
27 moments ( $M_0$ ,  $M_2$ ) and the mass concentrations of unidentified components (UIDs), BC, OA  
28 (POA plus SOA), dust (DU), sea salt (except chloride) (SS), sulfate, ammonium, nitrate,  
29 chloride and water are transported variables. By assuming a constant density of each chemical

1 composition, the  $M_3$  of each category was diagnosed. More detailed derivations and  
 2 descriptions of the modal moment approach are given in previous papers (e.g., Binkowski and  
 3 Shankar; 1995; Whitby and McMurry, 1997; Kajino, 2011). Only the final forms of the  
 4 equations, the time derivative terms of the moments, are shown in the current paper. **How**  
 5 **moments and the LNSD parameters are changed in the process operators are described later in**  
 6 **Sect. 2.2.10 and Fig. 2b.**

7

## 8 2.2.2 Intra-modal Brownian coagulation

9 The time derivative of moments due to intra-modal coagulation in the free-molecular regime  
 10 can be expressed as

11

$$\left. \frac{dM_0}{dt} \right|_{fm} = -bK_{fm} [M_0M_{0.5} + M_2M_{-1.5} + 2M_1M_{-0.5}] \quad (3a)$$

12

$$\left. \frac{dM_6}{dt} \right|_{fm} = 2bK_{fm} [M_3M_{3.5} + M_5M_{1.5} + 2M_4M_{2.5}] \quad (3b)$$

13 where  $K_{fm} = \left( \frac{3k_B T}{\rho_p} \right)^{0.5}$ ,  $k_B$  is the Boltzmann constant, T is temperature [K], and  $\rho_p$  is the  
 14 particle density.  $b$  is an approximation function of  $\sigma$  as

15

$$b(\sigma) = 1 + 1.2 \exp(-2\sigma) - 0.646 \exp(-0.35\sigma^2) \quad (4)$$

16 The time derivative terms in the near-continuum regime is

17

$$\left. \frac{dM_0}{dt} \right|_{nc} = -K_{nc} [M_0M_0 + M_1M_{-1} + A\lambda M_0M_{-1} + A\lambda M_1M_{-2}] \quad (5b)$$

18

$$\left. \frac{dM_6}{dt} \right|_{nc} = 2K_{nc} [M_3M_3 + M_4M_2 + A\lambda M_3M_2 + A\lambda M_4M_1] \quad (5b)$$

19 where  $K_{nc} = \frac{2k_B T}{3\mu}$ ,  $A=2.492$ ,  $\mu$  is the viscosity of air, and  $\lambda$  is the mean free path of air  
 20 molecules (cm). Finally, the harmonic mean of the time derivative terms in the free-molecular  
 21 and near-continuum regimes is applied to cover the full size range of aerosols as



1

$$\frac{dM_k}{dt} = \frac{dM_k}{dt} \Big|_{fm} \times \frac{dM_k}{dt} \Big|_{nc} \Big/ \left[ \frac{dM_k}{dt} \Big|_{fm} + \frac{dM_k}{dt} \Big|_{nc} \right] \quad (6)$$

2 During the intra-modal coagulation, the third moment proportional to the total volume  
3 remains unchanged,

4

$$\frac{dM_3}{dt} = 0 \quad (7)$$

### 5 2.2.3 Inter-modal Brownian coagulation

6 Rules for the transfer of the three moments and chemical mass concentrations from one mode  
7 to another must be predefined for the inter-modal coagulation calculations. These rules are  
8 listed in Table 3. Basically, the moments and masses are transferred from smaller/simpler  
9 categories into larger/multiple-component categories. Assuming that when a particle in mode  
10  $i$  coagulate with a particle in mode  $j$ , the merged particle goes into mode  $j$  (see Table 3), the  
11 time derivative terms of the moments in the near-continuum regime can be written as

12

$$\begin{aligned} \frac{dM_0^i}{dt} \Big|_{nc} &= -K_{nc} \left[ 2M_0^i M_0^j + M_1^i M_{-1}^j + M_{-1}^i M_1^j + A\lambda M_0^i M_{-1}^j + A\lambda M_{-1}^i M_0^j + A\lambda M_1^i M_{-2}^j + A\lambda M_{-2}^i M_1^j \right] \\ \frac{dM_3^i}{dt} \Big|_{nc} &= -K_{nc} \left[ 2M_3^i M_0^j + M_4^i M_{-1}^j + M_2^i M_1^j + A\lambda M_3^i M_{-1}^j + A\lambda M_2^i M_0^j + A\lambda M_4^i M_{-2}^j + A\lambda M_1^i M_1^j \right] \\ \frac{dM_6^i}{dt} \Big|_{nc} &= -K_{nc} \left[ 2M_6^i M_0^j + M_7^i M_{-1}^j + M_5^i M_1^j + A\lambda M_6^i M_{-1}^j + A\lambda M_5^i M_0^j + A\lambda M_7^i M_{-2}^j + A\lambda M_4^i M_1^j \right] \\ \frac{dM_0^j}{dt} \Big|_{nc} &= 0, \quad \frac{dM_3^j}{dt} \Big|_{nc} = -\frac{dM_3^i}{dt} \Big|_{nc} \\ \frac{dM_6^j}{dt} \Big|_{nc} &= K_{nc} \left[ 2M_6^i M_0^j + M_7^i M_{-1}^j + M_5^i M_1^j + A\lambda M_6^i M_{-1}^j + A\lambda M_5^i M_0^j + A\lambda M_7^i M_{-2}^j + A\lambda M_4^i M_1^j \right] \\ &\quad + 2K_{nc} \left[ 2M_3^i M_3^j + M_4^i M_2^j + M_2^i M_4^j + A\lambda M_3^i M_2^j + A\lambda M_2^i M_3^j + A\lambda M_4^i M_1^j + A\lambda M_1^i M_4^j \right] \end{aligned} \quad (8)$$

13

14

where  $M_k^i$  indicates the  $k$ th moment of mode  $i$ . In the free-molecular regime, the equations can  
be written as

1

$$\begin{aligned}
\left. \frac{dM_0^i}{dt} \right|_{fm} &= -bK_{fm} \left[ M_0^i M_{0.5}^j + M_{0.5}^i M_0^j + M_2^i M_{-1.5}^j + M_{-1.5}^i M_2^j + M_1^i M_{-0.5}^j + M_{-0.5}^i M_1^j \right] \\
\left. \frac{dM_3^i}{dt} \right|_{fm} &= -bK_{fm} \left[ M_3^i M_{0.5}^j + M_{3.5}^i M_0^j + M_5^i M_{-1.5}^j + M_{1.5}^i M_2^j + M_4^i M_{-0.5}^j + M_{2.5}^i M_1^j \right] \\
\left. \frac{dM_6^i}{dt} \right|_{fm} &= -bK_{fm} \left[ M_6^i M_{0.5}^j + M_{6.5}^i M_0^j + M_8^i M_{-1.5}^j + M_{4.5}^i M_2^j + M_7^i M_{-0.5}^j + M_{5.5}^i M_1^j \right] \\
\left. \frac{dM_0^j}{dt} \right|_{fm} &= 0, \quad \left. \frac{dM_3^j}{dt} \right|_{fm} = -\left. \frac{dM_3^i}{dt} \right|_{fm} \\
\left. \frac{dM_6^j}{dt} \right|_{fm} &= bK_{fm} \left[ M_6^i M_{0.5}^j + M_{6.5}^i M_0^j + M_8^i M_{-1.5}^j + M_{4.5}^i M_2^j + M_7^i M_{-0.5}^j + M_{5.5}^i M_1^j \right] \\
&\quad + 2bK_{fm} \left[ M_3^i M_{3.5}^j + M_{3.5}^i M_3^j + M_5^i M_{1.5}^j + M_{1.5}^i M_5^j + M_4^i M_{2.5}^j + M_{2.5}^i M_4^j \right]
\end{aligned} \tag{9}$$

2

where the approximation function  $b$ , newly proposed by Kajino (2011), is

3

$$\begin{aligned}
b &= 1 + 1.2\gamma \exp\left[-2\frac{\sigma_i + \alpha\sigma_j}{1 + \alpha}\right] - 0.646\gamma \exp\left[-0.35\frac{\sigma_i^2 + \alpha\sigma_j^2}{1 + \alpha}\right] \\
\gamma &= \left[1 - \frac{\sqrt{1 + \alpha^3}}{1 + \sqrt{\alpha^3}}\right] \bigg/ \left[1 - \frac{1}{\sqrt{2}}\right], \quad \alpha = \frac{D_{gj}}{D_{gi}}
\end{aligned} \tag{10}$$

4 The harmonic mean of the time derivative terms (Eq. 6) is applied to cover the full size range.

#### 5 2.2.4 Number concentration of soot collided to coarse mode particles

6 Soot particles sometimes form internal mixture with coarse mode particles such as dust and  
7 sea salt particles, and such mixtures alter optical properties of the coarse mode particles  
8 significantly and contribute to atmospheric solar heating and surface dimming (Clarke et al.,  
9 2004; Zhu et al., 2007; Guazzotti et al., 2011). Such mixtures can be predicted in the RAQM2  
10 model as BC mass and  $M_0^{AGR}$  number concentrations in the COR category (Table 2).  $M_0^{AGR}$   
11 indicates the number concentration of soot particles (AGR) collided with COR particles and is  
12 calculated as

$$\left. \frac{dM_0^{AGR}}{dt} \right|_{coag} = \left. \frac{dM_0}{dt} \right|_{coag}^{COR-AGR} \tag{11}$$

14  $M_0^{AGR}$  exceeds the  $M_0$  of COR because  $M_0^{AGR}$  does not indicate the number of COR particles  
15 internally mixed with soot but indicates the number of times each AGR particle hits COR  
16 particles. Brownian coagulation theory assumes the coalescence efficiency is unity, but it may

1 not be true for the atmospheric aerosols. The efficiency of the bouncing/sticking of colliding  
 2 atmospheric particles should be formulated.

3

#### 4 2.2.5 Condensation

5 The zeroth moment  $M_0 (=N)$  remains constant during the condensation process.

6

$$\frac{dM_0}{dt} = 0 \quad (12)$$

7 The condensational growth of the particle mass  $M$  of each **mode** can be expressed as

8

$$\frac{dM}{dt} = \int \frac{m_{w,p}}{m_{w,g}} (c_\infty - c_s) \psi(d_p) n(d_p) dd_p \quad (13)$$

9 where  $m_{w,p}$  and  $m_{w,g}$  represent the molecular weights of semi-volatile components in the  
 10 particle and gas phases, respectively, and  $c_\infty$  and  $c_s$  are the gas phase concentrations in the  
 11 bulk phase (near the aerosol surface) and those on the aerosol surface, respectively. The  $\psi$ s are  
 12 different in the free-molecular and the near continuum regimes, which can be written as

13

$$\psi^{fm}(d_p) = \frac{\pi \alpha \bar{c}}{4} d_p^2 \quad (14a)$$

14

$$\psi^{co}(d_p) = 2\pi D_v d_p \quad (14b)$$

15 respectively, where  $\alpha$  is a mass accommodation coefficient assumed constant as 0.1,  $\bar{c}$  is a  
 16 mean velocity of the gas molecules, and  $D_v$  is the molecular diffusion coefficient. Using the  
 17 harmonic mean approach to cover the two regimes, the time derivative term of arbitrary  
 18 moments due to condensation can be rewritten as

19

$$\frac{dM_k}{dt} = \frac{1}{\rho_p} \frac{m_{w,p}}{m_{w,g}} (c_\infty - c_s) \left| \frac{k\alpha\bar{c}}{2} M_{k-1}, 4kD_v M_{k-2} \right|_{harm} \quad (15)$$

20 where  $|A,B|_{harm}$  indicates the harmonic mean of A and B and, thus,  $AB/(A+B)$ . The  
 21 condensational growth of mass is expressed as

22

$$\frac{dM}{dt} = \frac{\pi \rho_p}{6} \frac{dM_3}{dt} \quad (16)$$

1 To obtain the gas phase concentrations on the aerosol surface  $c_s$ , which is thermodynamically  
 2 equilibrated, ISORROPIA II (Fountoukis and Nenes, 2007) and Edney et al. (2007) are used  
 3 for semi-volatile inorganic and organic compounds, respectively.

4

## 5 2.2.6 Simultaneous solution of nucleation, condensation and mode merging

6 RAQM2 achieved a completely dynamic (non-equilibrium) solution of a gas-to-particle mass  
 7 transfer over a wide range of aerosol diameters from 1 nm to super-micrometer size. The new  
 8 particle formation (NPF) process is, however, not dynamically solved, but parameterized,  
 9 which is inevitable for the time and spatial scales of the simulation. Recently, numerous NPF  
 10 parameterizations have been proposed based on laboratory experiments, theoretical and  
 11 molecular dynamics calculations, and nanoparticle observations (Kulmala and Kerminen,  
 12 2008; Hirsikko et al., 2011). However, numerous uncertainties and discrepancies remain  
 13 among each parameterization (Zhang et al., 2010). Therefore, we used the parameterizations  
 14 based on several observations in diverse atmospheric locations (Kuang et al., 2008) to obtain  
 15 the plausible nucleation rates for realistic conditions.

16 To solve the condensation onto the pre-existing particles and the nucleation of sulfuric acid  
 17 gas, the operator and time splitting method was applied. The nucleation and condensation  
 18 processes were solved simultaneously using the short split time step ( $\Delta t$ ) of 1 sec with an  
 19 explicit method (forward in time) (see Section 2.2.9 and Fig. 2a). We found that a 1-sec time  
 20 step was sufficient to yield an accurate nucleation rate under the realistic conditions of  
 21 sulfuric acid gas up to  $10^8$  molecules ( $\text{cm}^{-3}$ ) and aerosol number concentrations from  $10^2$  to  
 22  $10^6$  ( $\text{cm}^{-3}$ ) using the Kuang et al. (2008) parameterization. When nucleation occurs, the  
 23 number of new particles, produced within 1 sec, with a  $D_g$  and  $\sigma$  of 1 nm and unity,  
 24 respectively, were entered in the ATK category. Because the ATK particles swelled rapidly  
 25 due to condensation and Brownian coagulations, the aerosols were merged to the larger  
 26 particle category ACM, as shown in Table 3. The portion of the  $k$ th moment larger than a  
 27 criteria diameter  $D_c$  were readily calculated using the error function  $\text{erf}(x)$  as

28

$$\left[ M_k \right]_{D_c} = \int_{\ln D_c}^{\infty} D^k n(\ln D) d \ln D = \frac{M_k}{2} \left[ 1 - \text{erf} \left( \frac{\ln D_c - \ln D_g - k \ln^2 \sigma}{\sqrt{2} \ln \sigma} \right) \right] \quad (17)$$

1 The portion of mass is identical to that of the third moment. Each moment and each mass of  
2 the chemical compositions in ATK exceeding  $D_c$  (set as 40 nm in the study) were merged into  
3 the ACM category using Eq. (17), and vice versa: when the shrinking of the ACM occurs, the  
4 portion of the moments and mass smaller than 40 nm are merged to ATK (Table 3).

5

### 6 2.2.7 Grid-scale and sub-grid-scale wet deposition

7 For the grid-scale wet deposition, the CCN activation and subsequent cloud microphysical  
8 processes were parameterized using Abdul-Razzak and Ghan (2000) and WSM6 (Lin et al.,  
9 1983). When the Abdul-Razzak and Ghan (2000) parameterization predicts that CCN  
10 activation occurs in a grid cell, the portions of the moments and the mass (see Eq. (17)) were  
11 transferred to the grid-scale cloud droplets. Lin et al. (1983) developed an explicit cloud  
12 microphysics model in which interactions between cloud droplets and other hydrometers,  
13 such as rain, snow and graupel droplets, are formulated. The autoconversion rate (cloud  $\rightarrow$   
14 rain) and the accretion rate of cloud droplets by rain, snow, and graupel (cloud  $\rightarrow$  rain, cloud  
15  $\rightarrow$  snow, cloud  $\rightarrow$  graupel), predicted by WSM6, were used to calculate the transfer of the  
16 aerosol moments and mass in the cloud droplets to the other hydrometers.

17 Particles such as hydrophobic forms of dust and soot efficiently act as IN in ice and mixed  
18 phase clouds. Pagels et al. (2009) found that a mass increase of 2-3 times by the condensation  
19 of water and sulfuric acid onto soot agglomerates resulted in a transformation to spherical  
20 shapes. We assumed here that the soot loses IN activity after the growth by condensation.  
21 Thus, hydrophobic particles in RAQM2 are defined as AGR and COR categories when the  
22 hygroscopic mass (=sum of  $\text{SO}_4^{2-}$ ,  $\text{NH}_4^+$ ,  $\text{NO}_3^-$ ,  $\text{Cl}^-$  and SS) is less than 50% of the total dry  
23 mass, i.e., the hygroscopic mass is less than the hydrophobic mass (=sum of UIC, BC, OA  
24 and DU).

25 All components in OA were assumed to be hydrophobic here, although some of the secondary  
26 OA was hydrophilic. For the IN activation of aerosols, we used the parameterizations of  
27 Lohmann and Diehl (2010) for contact freezing and immersion (+condensation) freezing. We  
28 assumed that the IN activation occurred only in a grid cell that contains ice particles predicted  
29 by WRF with a temperature lower than  $-3^\circ\text{C}$ . The fractions of frozen droplets for dust and  
30 soot particles are assumed as functions of temperature based on Fig. 1 of Lohmann and Diehl  
31 (2010), respectively, as follows:

$$\begin{aligned}
F_{cn\_du} &= -14(T_c + 3) \\
F_{cn\_bc} &= -15(T_c + 10) \\
F_{im\_du} &= -0.1(T_c + 27) \\
F_{im\_bc} &= -0.5(T_c + 36)
\end{aligned}
\tag{18}$$

where  $F_{cn\_du}$ ,  $F_{cn\_bc}$ ,  $F_{im\_du}$ , and  $F_{im\_bc}$  represent the fractions for the contact freezing of hydrophobic COR and AGR and the immersion freezing of hydrophobic COR and AGR, respectively, and  $T_c$  is the grid air temperature ( $^{\circ}\text{C}$ ). For immersion freezing, the  $F_{im\_du}$  and  $F_{im\_bc}$  are the exact fractions scavenged into ice particles. For contact freezing, some portion of  $F_{cn\_du}$  and  $F_{cn\_bc}$  actually coagulated with ice or super-cooled cloud droplets can be scavenged into ice particles. The Brownian coagulation of hydrophobic COR and AGR with cloud ice/water droplets was calculated using the inter-modal coagulation Eqs. (6), (8), (9) and (10). To obtain the size distribution of cloud ice/water droplets, we assumed a simple Khrgian-Mazin-type gamma size distribution (Pruppacher and Klett, 1997):

$$n(a) = Aa^2 \exp(-Ba) \tag{19}$$

where  $n(a)$  is the number size distribution function,  $A$  and  $B$  are parameters related to moments of the distribution, and  $a$  is a particle radius. This Khrgian-Mazin equation is almost identical to the LNSD, with a standard deviation of approximately 1.64. Thus, assuming a  $D_g$  of cloud ice/water droplets of  $15 \mu\text{m}$  together with cloud ice/water mixing ratios and their density, the size distribution can be fixed for the inter-modal Brownian coagulation. Subsequently, aerosols in ice particles are converted to snow via autoconversion (aggregation) and are converted to rain, snow and graupel particles due to accretion, with conversion rates predicted by the explicit cloud microphysics parameterization (WSM6).

The below-cloud scavenging process is considered inter-modal coagulation with falling hydrometers, such as rain, snow and graupel droplets. Kajino and Kondo (2011) deduced the collision/coalescence equations due to gravitational settling in Eqs. (A37)-(A43) in section A.4 of their paper. The LNSD is assumed in their equations, while the size distributions of such hydrometers are often represented by a gamma function. Thus, we first derive the gamma size distributions (GSDs) of the hydrometers as a function of the mixing ratio (Hong and Lin, 2006) and then yield the LNSD converted from GSD, preserving the three moments.

1 Once captured in the hydrometeors in either ways, a certain portion of the moments and  
2 chemical components is assumed to immediately reach the ground in the same manner as  
3 Eqs.(1) and (2) in Kajino and Kondo (2011).

4

#### 5 2.2.8 Dry deposition and gravitational sedimentation

6 The dry deposition and gravitational sedimentation processes are formulated in the same  
7 manner as that given in Appendices 5 and 6 of Kajino and Kondo (2011) through Eqs. (A44)  
8 to (A48). With regard to the calculation of dry deposition for particles, however, the original  
9 parameterization of surface resistance by Zhang et al. (2001) used in Kajino and Kondo  
10 (2011) was modified based on comparisons using observational data by more recent works  
11 (Katata et al. 2008, 2011; Petroff and Zhang 2010) to improve the prediction accuracy of dry  
12 deposition. In the present paper, four important revisions were performed:

- 13 1. On the assumption that forests have tall canopies and a large leaf surface area that enables  
14 a large amount of particles from the atmosphere to be captured, the empirical constant  $\varepsilon_0$   
15 in Zhang et al. (2001) was set to 5 and 1 for the categories of forest and short vegetation,  
16 respectively. This modification decreases the surface resistance, resulting in large values  
17 of dry deposition velocity for forest compared with other vegetation.
- 18 2. For the collection efficiency by leaves due to inertial impaction, the modified function of  
19 Peters and Eiden (1992) (Eq. (7) in Katata et al. 2008) was used. The function was  
20 validated with the data of fog deposition ( $> 1 \mu\text{m}$ ) onto coniferous and broad-leaved  
21 forests in Katata et al. (2008).
- 22 3. Collection efficiencies due to interception and Brownian diffusion by Kirsch and Fuchs  
23 (1968) and Fuchs (1964) (Eqs. (14) and (16) in Katata et al. 2011), respectively, were also  
24 used for vegetative surfaces. Those formulations were verified using the flux data of fine  
25 aerosols ( $< 1 \mu\text{m}$ ) over the coniferous forest in Katata et al. (2011).
- 26 4. For the land use categories of desert, tundra, ice cap and glacier, inland water, and ocean,  
27 the surface resistance for non-vegetated surfaces proposed by Petroff and Zhang (2010)  
28 were adopted.

29 After the above modifications, the dry deposition velocity calculated by the modified model  
30 agreed better with the observational data than the original model of Zhang et al. (2001). For

1 example, the size-segregated dry deposition velocity for the vegetative surface decreased and  
 2 increased by one order of magnitude within a 0.1- and 1- $\mu\text{m}$ -diameter range, which is  
 3 comparable to the performance of the detailed multi-layer particle deposition model by Katata  
 4 et al. (2011). For ground and water surfaces, a good agreement between calculations by the  
 5 modified model and observations from the literature was found, as shown in Petroff and  
 6 Zhang (2010).

7

## 8 2.2.9 Operator splitting and time splitting for aerosol dynamical modeling

9 The operator splitting and time splitting used for the aerosol dynamics module are illustrated  
 10 in Fig. 2a. In the flow chart, each solid box indicates each operator, and the arrows denote the  
 11 order of operator calculations.  $\Delta T_{\text{host}}$  is the longest time step of the host calculation, i.e.,  
 12 horizontal advection and diffusion. In this study, we set  $\Delta x = 60$  km, so  $\Delta T_{\text{host}}$  is set as 300 sec  
 13 after optimization of the CPU time and the deficit of numerical diffusions.  $\Delta t$  is a split time  
 14 step within each operator calculation, whereas the  $\Delta T$ s denote the integrated time steps of  
 15 each operator before stepping forward to the next operator. First, the production rate of  
 16 sulfuric acid gas via homogeneous (gas phase) chemistry was calculated using SAPRC99 with  
 17 the Eulerian Backward Iteration method with  $\Delta t = 150$  sec. The production rate of sulfuric  
 18 acid gas was obtained as  $\Delta C_{\text{H}_2\text{SO}_4} / \Delta T_{\text{host}}$ . The nucleation rate  $J_{1\text{nm}}$  (Kuang et al., 2008) and  
 19 the condensation rate (Eqs. 15 and 16) were calculated using  $C_{\text{H}_2\text{SO}_4} = \Delta C_{\text{H}_2\text{SO}_4} / \Delta T_{\text{host}} \times \Delta t$  (=1  
 20 sec). Then, the gas-phase concentration  $C_{\text{H}_2\text{SO}_4}$  was distributed into the ATK category to  
 21 produce new particles and into all categories by condensation simultaneously. After finishing  
 22 the NPF&Cond. operator, the intra- and inter-category Brownian coagulation was solved with  
 23 an arbitrary split time to integrate for  $0.5\Delta T_{\text{host}}$  (150 sec). CFL-like conditions were  
 24 established for Brownian coagulation as

$$25 \quad t_{\text{CFL}} = M_0^i \left/ \frac{dM_0^i}{dt} \right. \quad (20)$$

26 where  $\Delta t$  is set as the maximum so that it never exceeds  $0.5 \times t_{\text{CFL}}$  for all the **modes in the**  
 27 **categories** due to intra- and inter-category coagulations. After the Coag. operator is calculated  
 28 for half the host time step, the condensation of the semi-volatile inorganic and organic  
 29 components is calculated. The CFL conditions are also introduced for the condensation  
 30 process as



1  $t_{CFL} = 1/k_w$  (21)

2 where  $k_w$  is the mass-transfer coefficient ( $s^{-1}$ ) for each **mode** defined as

3 
$$k_w = \frac{dM}{dt} \frac{1}{(c_\infty - c_s)}$$
 (22)

4 and the time derivative of mass concentration  $dM/dt$  is obtained from Eqs. (15) and (16).  $\Delta t$  is  
5 set as the maximum so that it never exceeds  $0.1 \times t_{CFL}$  for all **modes of the** categories. The  
6 condensation process was integrated for the host time step period (300 sec) with the arbitrary  
7 time step. After the volatile components condensation operator, the Coag. operator was  
8 calculated again for the remaining half of the host time step (150 sec). Other processes then  
9 follow, including sedimentation, dry deposition, subgrid-scale wet deposition, grid-scale CCN  
10 activation and cloud microphysics.

11 Strictly speaking, NPF, the condensation of sulfuric acid gas and other semi-volatile  
12 components, and Brownian coagulation should be solved with the smallest time step, i.e., 1  
13 sec, to calculate the growth of aerosol particles consistently. However, although  
14 ISORROPIA2 is computationally efficient compared with other models (Fountoukis and  
15 Nenes, 2007), solving the thermodynamic equilibrium state among multi-component species  
16 for every 1 sec for all **modes of the** categories in the regional scale simulation is still far from  
17 feasible for our computational resources. To avoid operator split problems to some extent, the  
18  $\Delta T$  of the Brownian coagulation is divided in two and inserted separately between the two  
19 condensational operators in the current implementation of the model.

20

#### 21 **2.2.10 Time evolution of the moments and the LNSD parameters in each process** 22 **operator**

23 At any steps during the time integration, each mode of the categories has the specific size  
24 parameters ( $N, D_g, \sigma_g$ ) to characterize their LNSD. Then  $M_0$  and  $M_2$  derived by Eq. 2, together  
25 with the chemical components (listed in Table 2) are transported via advection, turbulent  
26 diffusion, and sub-grid scale convection. Then, there are three moments after the transport  
27 operator,  $M_0, M_2$  and  $M_3$ , which is diagnosed by total mass and predetermined density of each  
28 chemical component. Using the three moments, the size parameters ( $N, D_g, \sigma_g$ ) after the  
29 transport operators are obtained by Eq. 2. This is the case for the transport operators but in

1 common for the aerosol process operators (Fig. 2a) too, as illustrated in Fig.2b. To obtain  
2  $dM_0/dt$ ,  $dM_2/dt$ , and  $dM_3/dt$  for the condensation operator in Eq.15, any moments necessary in  
3 the equation are derived by the size parameters. Using Eq.15,  $M_0$ ,  $M_2$  and  $M_3$  after the  
4 condensation operator are obtained, and subsequently  $N$ ,  $D_g$  and  $\sigma_g$  after the operator. The  
5 same procedure is applied for other process operators such as sedimentation, dry deposition,  
6 subgrid-scale wet deposition, grid-scale CCN activation and cloud microphysics, except for  
7 the coagulation operator, where  $dM_6/dt$  needs to be calculated instead of  $dM_2/dt$  (Eqs.3–10).  
8 In the coagulation operator too, any moments necessary for the coagulation equations (Eqs.3–  
9 10) are derived by the size parameters  $N$ ,  $D_g$  and  $\sigma_g$  before the coagulation operator,  $M_0$ ,  $M_3$   
10 and  $M_6$  after the coagulation operator is obtained by the equations, and then  $N$ ,  $D_g$  and  $\sigma_g$  after  
11 the coagulation operator are derived. We set the minimum  $\sigma_g$  value of 1.0 and the maximum  
12 values of 1.7 for ATK, ACM and AGR and 2.0 for COR to avoid unrealistic values. When  $\sigma_g$   
13 exceeds the either limits,  $\sigma_g$  is adjusted to the limit values preserving  $M_0$  and  $M_3$  (thus  $M_2$  is  
14 changed accordingly).

15

## 16 3 Model evaluation using observation data

### 17 3.1 EANET monitoring network data

18 Acid Deposition Monitoring Network in East Asia (EANET) data were used for model  
19 evaluation. The guidelines, technical documents, monitoring reports and quality assurance  
20 and quality control programs are available at <http://www.eanet.cc/product.html>. We used  
21 hourly  $\text{SO}_2$ ,  $\text{NO}_x$ ,  $\text{O}_3$ ,  $\text{PM}_{2.5}$  and  $\text{PM}_{10}$  concentrations and meteorological parameters, and 1-  
22 or 2- weekly concentrations of gases ( $\text{SO}_2$ ,  $\text{NH}_3$ ,  $\text{HNO}_3$ , and  $\text{HCl}$ ) and aerosols components  
23 ( $\text{SO}_4^{2-}$ ,  $\text{NO}_3^-$ ,  $\text{Cl}^-$ ,  $\text{NH}_4^+$ ,  $\text{Na}^+$ ,  $\text{Mg}^{2+}$ ,  $\text{K}^+$ , and  $\text{Ca}^{2+}$ ) using the filter pack method (FP). The  
24 long-duration sampling of FP causes several artifact problems; volatilization of  $\text{NH}_4\text{NO}_3$  and  
25  $\text{NH}_4\text{Cl}$  collected on a filter occur during sampling and/or high humidity may reduce measured  
26 gas concentration due to trapping by condensed water in the filter pack. To avoid the  
27 problems, only total nitrate (T- $\text{NO}_3^-$ ;  $\text{HNO}_3^-$  gas plus  $\text{NO}_3^-$  aerosol), total ammonium (T-  
28  $\text{NH}_4^+$ ;  $\text{NH}_3$  gas plus  $\text{NH}_4^+$  aerosol), and total chloride (T- $\text{Cl}^-$ ;  $\text{HCl}$  gas plus  $\text{Cl}^-$  aerosol) are  
29 used for in this study.

1 To obtain the anthropogenic  $\text{SO}_4^{2-}$  and  $\text{Ca}^{2+}$  originating from the Asian dust (calcite), nss-  
2  $\text{SO}_4^{2-}$  and nss- $\text{Ca}^{2+}$  were defined, excluding the contribution of sea salt using a standard mean  
3 chemical composition of sea water (DOE, 1994), as follows:

$$4 \quad [\text{nss-SO}_4^{2-}] = [\text{SO}_4^{2-}] - 0.251 \times [\text{Na}^+] \quad (23)$$

$$5 \quad [\text{nss-Ca}^{2+}] = [\text{Ca}^{2+}] - 0.038 \times [\text{Na}^+] \quad (24)$$

6 where [ ] denotes the weight concentrations in  $\mu\text{g m}^{-3}$ .

7 Among the EANET stations, six stations in Japan are selected for the model evaluation, as  
8 depicted in Fig. 1 and listed in Table 4. The red triangles denote the stations located on small  
9 islands or isolated capes in down-wind regions. These stations were situated in areas without  
10 nearby large anthropogenic emission sources and without the complexity of local orographic  
11 winds; therefore, high concentration episodes mostly coincided with synoptic-scale  
12 disturbances and were well simulated by regional-scale models. On the other hand, because  
13 those stations were very close to ocean surfaces, the regional-scale simulations of ocean-  
14 originated species such as sea salt did not often agree well with the observations. We often  
15 obtained a better agreement for sea salt-originated components at inland or mountainous  
16 stations.

17

### 18 3.2 Q-AMS aerosol observation data at the CHAAMS site

19 Because the temporal resolution of the ionic aerosol component measurements of EANET is 2  
20 weeks, the simulated transport and transformation of aerosol components cannot be evaluated.  
21 Alternatively, we used the hourly concentrations of  $\text{PM}_1\text{-nss-SO}_4^{2-}$ ,  $\text{PM}_1\text{-NO}_3^-$ ,  $\text{PM}_1\text{-Cl}^-$ , and  
22  $\text{PM}_1\text{-NH}_4^+$  (50% cutoff of aerosols with an aerodynamic diameter of  $1 \mu\text{m}$ ), measured using a  
23 quadrupole aerosol mass spectrometer (Aerodyne Research Inc., Q-AMS) at the Cape Hedo  
24 Atmospheric and Aerosol Monitoring Station (CHAAMS) site (Takami et al., 2007;  
25 Takiguchi et al., 2008). The CHAAMS site is located within the same premises as the  
26 EANET Hedo station.

27

### 1 3.3 Bulk mass concentrations of gaseous species

2 It was necessary to predict the O<sub>3</sub> concentration precisely because it is an important oxidizing  
3 agent in the atmosphere for secondary aerosol formations. This prediction was also important  
4 because O<sub>3</sub> is a source of the most efficient oxidants in the troposphere, OH radicals. Because  
5 O<sub>3</sub> is a relatively longer-lived species, the contribution of inter-continental transport and  
6 stratospheric ozone intrusion is substantial (Sudo and Akimoto, 2007; Nagashima et al., 2010).  
7 Consequently, the seasonal trends can never be reproduced by a tropospheric regional-scale  
8 model itself without appropriate seasonal variations of the lateral and upper (tropopause)  
9 boundary conditions. Therefore, we used the climatological simulation results of monthly  
10 NO<sub>x</sub>, O<sub>x</sub>, CO and VOCs concentrations using a global-scale stratospheric and tropospheric  
11 chemistry-climate model (MRI-CCM2; Deushi and Shibata, 2011) as the boundary conditions  
12 of RAQM2.

13 Table 5 summarizes the statistical analysis for the comparison between the observation and  
14 simulation of all the available data at the six EANET stations. The simulation of daily  
15 maximum 8-hour mean O<sub>3</sub> was found to be successful, as the medians of observation and  
16 simulation were close to each other and the Root Mean Square Errors (RMSEs) were much  
17 lower than the medians. The correlation coefficient R is 0.47 and 96% of the data-satisfied  
18 factor of 2. The R of the daily mean SO<sub>2</sub> and NO<sub>x</sub> concentrations was the same as that of O<sub>3</sub>,  
19 whereas there were larger discrepancies in the medians, RMSEs, FAC2 and FAC5. Because  
20 these EANET stations are located over remote ocean areas, the temporal variations of O<sub>3</sub> were  
21 always incremented by background concentrations due to the long-range transport. While this  
22 smaller variation/background ratio of O<sub>3</sub> resulted in better scores for RMSEs, FAC2 and  
23 FAC5 than SO<sub>2</sub> and NO<sub>x</sub>, the same levels of R indicate that the predictability of the transport  
24 patterns of the three species were similar. The simulated O<sub>3</sub> was not biased toward the  
25 observation, but the simulated SO<sub>2</sub> and NO<sub>x</sub> were biased by 30-50%.

26

### 27 3.4 Bulk mass concentrations of aerosol chemical components

28 Fig. 3 presents a scatter diagram between the observed and modeled concentrations of  
29 biweekly chemical components at the Rishiri, Oki and Hedo stations. These stations are  
30 located over a wide range, from the northeast to the southwest of the Japan archipelago, so  
31 different types of long-range transport patterns from the Asian continent can be evaluated. We

1 also selected these stations because the  $PM_{2.5}$  mass concentrations were monitored together  
2 with  $PM_{10}$  only at Rishiri and Oki and because the AMS  $PM_1$  measurements were taken only  
3 at Hedo.

4 The statistics of the corresponding data at all six stations are listed in Table 5. The medians of  
5 the modeled  $nss-SO_4^{2-}$  and  $T-NH_4^+$  were approximately 30% smaller than the observed,  
6 whereas the modeled  $T-NO_3^-$  was almost double that observed. The nitric acid and ammonia  
7 are semi-volatile in atmospheric conditions and were partitioned into gas and aerosol phases.  
8 However, due to the artifact problems mentioned in Sect. 3.1, the gas-aerosol partitioning was  
9 not evaluated. The partitioning is essentially important for the transport of the species because  
10 the dry and wet deposition efficiencies of nitric acid and ammonia in gas and aerosol phases  
11 are very different (Kajino et al., 2008). The modeled gas-aerosol partitioning of the semi-  
12 volatile components should be evaluated using accurate measurements for  $HNO_3$  and  $NH_3$   
13 gases in the future to identify the possible causes of the discrepancies between the model and  
14 observation. The RMSEs of  $nss-SO_4^{2-}$ ,  $NH_4^+$ , and  $NO_3^-$  were comparable to the medians, and  
15 the  $R^2$  values were always greater than 0.5.

16  $T-Cl^-$  and  $Na^+$  mainly originate from sea salt particles because the EANET stations are close  
17 to the ocean. Natural aerosols are usually difficult to simulate due to the large uncertainties in  
18 the emission flux estimations, and the Rs were lower than the other chemical components.  
19 Still, the RMSEs and modeled medians were close to the observed medians.  $nss-Ca^{2+}$  was  
20 considered to originate from Asian dust particles, which contain calcite; these are also natural  
21 aerosols and were difficult to simulate. The modeled median was approximately double that  
22 measured. We assumed uniform compositions for dust emission from the whole model  
23 domain, which may not have been natural. Still, a large value of R was obtained for  $nss-Ca^{2+}$   
24 because the long-range transport of Asian dust in Japan is most influential in spring, and this  
25 feature was well reproduced by RAQM2. The Rs at the western stations, where the dust  
26 transport is more frequent, were especially larger, with 0.74 and 0.76 at Hedo and Oki,  
27 respectively.

### 28 3.5 Size distributions of total aerosol mass

29 Fig. 4 presents the daily mean observed and modeled concentrations of  $PM_{10}$ ,  $PM_{2.5}$ , and  
30  $PM_{2.5}/PM_{10}$  concentration ratios and modeled constituent fractions of  $PM_{10}$ ,  $PM_{2.5}$ , and  $PM_1$  at  
31 the Rishiri and Oki stations.  $PM_{2.5}$  includes sub-micron aerosols and a portion of super-

1 micron aerosols, such as sea salt and dust particles, so the  $PM_{2.5}/PM_{10}$  ratio provided some  
2 idea of the mass size distribution of the super-micron particles or mass ratios of anthropogenic  
3 (mostly sub-micron) and natural origin aerosols (mostly super-micron) (Kajino and Kondo,  
4 2011). Notably, the modeled  $PM_{2.5}$  and  $PM_{10}$  were derived using Eq. (17) by cutting each wet  
5 aerosol **particles in a category** at the exact diameter (2.5 and 10  $\mu m$ , respectively), so the size  
6 classification property differed from that of the instruments, characterized by the so-called  
7 cut-off curve. As shown in Table 5, the medians of the modeled  $PM_{2.5}$  and  $PM_{10}$  are 40% and  
8 50% smaller, respectively, than the observed. The RMSEs were comparable to the median  
9 values, and approximately half of the data satisfied a factor of 2 and more than 80% satisfied  
10 a factor of 5. Notably, the statistics for  $PM_{10}$  included data from all six stations, whereas those  
11 for  $PM_{2.5}$  included only those from Oki and Rishiri. The modeled and observed median of the  
12  $PM_{2.5}/PM_{10}$  ratio agreed well, as the RMSE is small and more than 80% of the data satisfied a  
13 factor of 2, except that R is almost zero. Together with the comparison shown in Figs. 4e and  
14 4f, the daily variations of the  $PM_{2.5}/PM_{10}$  ratio may have failed to be simulated, but longer-  
15 term features were well reproduced by the model. The variations of the measured ratios were  
16 not large, with the median ranging from 0.4 to 0.6. The values at Oki (0.9) in August were  
17 excluded because the measured  $PM_{2.5}$  data were missing during most of the period. The  
18 modeled mean  $PM_{2.5}/PM_{10}$  ratios were also within the same range of 0.4-0.6, except at Rishiri  
19 from January to March. The overestimation of the model during the period indicates that the  
20 modeled size was smaller than that observed.

21 The 10-d mean fractions of the  $PM_{10}$ ,  $PM_{2.5}$ , and  $PM_1$  constituents are also shown in Fig. 4  
22 (g)-(l). The red, green, yellow, blue, and sky blue columns indicate the total dry mass of ATK  
23 and ACM, the total dry mass of AGR, the dust mass (DU) of COR, the sea salt mass ( $SS+Cl^-$ )  
24 of COR, and the other dry mass of COR, respectively. The ATK, ACM, and AGR are mainly  
25 of anthropogenic origin and are composed of submicron particles ( $PM_1$ ). COR is mainly of  
26 natural origin and was partitioned into  $PM_{2.5}$  and  $PM_{10}$ . The ATK, ACM, and AGR particles  
27 accounted for more than 90% of the  $PM_1$  except in spring and autumn at Rishiri and spring at  
28 Oki. The COR particles accounted for more than 90% of the  $PM_{10}$  except in summer. The  
29 modeled fractions of ATK, ACM, and AGR in  $PM_{2.5}$  and  $PM_{10}$  became larger in summer  
30 because the sea salt production and dust transport are less pronounced than those in the cold  
31 seasons. The  $PM_{2.5}/PM_{10}$  ratio of the chemical components was an excellent indicator of the  
32 mixing type of the inorganic components (Kajino and Kondo, 2011), but that of the total  
33 aerosol mass was merely an indicator of the COR category sizes. The modeled fractions of the

1 constituents of  $PM_{2.5}$  and  $PM_{10}$  did not differ greatly from one another, but those of  $PM_1$  and  
2  $PM_{10}$  were very different. Unfortunately, we did not obtain  $PM_1$  mass concentration data, but  
3 a comparison between the modeled and observed  $PM_1/PM_{10}$  ratio, if available, may provide  
4 additional important implications for modeling studies.

5

## 6 3.6 Size distributions and mixing types of inorganic components

7

### 8 3.6.1 Relationship between chemical size distribution and mixing types

9 Fig. 5 shows the observed and modeled (left) daily mean  $PM_1$  concentrations of the  $nss-SO_4^{2-}$ ,  
10  $NH_4^+$ ,  $NO_3^-$ , and  $Cl^-$  concentrations and (right) the biweekly mean bulk concentrations of  $nss-$   
11  $SO_4^{2-}$ ,  $T-NH_4^+$ ,  $T-NO_3^-$ ,  $T-Cl^-$ ,  $Na^+$ , and  $nss-Ca^{2+}$ . To derive the modeled  $PM_1$  concentrations  
12 for the comparisons with the AMS data, Eq. (17) was again applied. Notably, the equation  
13 was applied for the modeled “dry” size distribution, whereas it was applied for the “wet” size  
14 distribution for the cases of  $PM_{2.5}$  and  $PM_{10}$ , corresponding to the measurement techniques.

15 Table 6 summarizes the statistical analysis of the corresponding data shown in Fig. 5. In  
16 summer, the Pacific high is influential, carrying a clean maritime air mass to Hedo. In cold  
17 seasons, long-range transport from the Asian continent via cyclonic fronts or anticyclones  
18 propagating eastward is predominant. Therefore, the concentrations of air pollutants are low  
19 in summer and high in spring, autumn, and winter. These seasonal features and daily  
20 variations were successfully reproduced by the model. The model results of the natural  
21 aerosols, such as sea salt ( $Na^+$ ) and Asian dust ( $Ca^{2+}$ ), at Hedo were also successful. The  
22 transport events of the Asian dust in spring and autumn were found in both the observation  
23 and simulation.

24 Although the variations were well simulated, the levels were underestimated for some  
25 components, such as  $PM_1-nss-SO_4^{2-}$  and  $PM_1-NH_4^+$ . The modeled medians were  
26 approximately 30% of those observed (Table 6). The model also underestimated the bulk  $nss-$   
27  $SO_4^{2-}$  and  $T-NH_4^+$ , and the underestimation was consistent with that for  $PM_1$ . The  
28 underestimations of  $PM_1-nss-SO_4^{2-}$  and  $PM_1-NH_4^+$  were most likely due to the  
29 underestimation of the bulk mass. The trends and values of  $PM_1-NO_3^-$  were well predicted by  
30 the model, whereas the  $T-NO_3^-$  was overestimated.

1 Fig. 6 presents the (left) biweekly mean  $PM_1$  to the total (gas plus aerosol) concentration  
2 ratios for  $nss-SO_4^{2-}$ ,  $T-NH_4^+$ ,  $T-NO_3^-$ , and  $T-Cl^-$ . The observed values were depicted only  
3 when the available hourly AMS data exceeded 50% during each biweekly FP period (more  
4 than 140 hourly data out of the two weeks). The statistical values between the observed and  
5 modeled data are listed in Table 6. Fig. 6 also presents (right) the biweekly mean fractions of  
6 gas and aerosol categories for each inorganic component. The observed median of the  $PM_1$  to  
7 bulk  $nss-SO_4^{2-}$  ratio was 0.85. The ratio exceeded 1.0 for some cases, so it may be within the  
8 uncertainties of the analysis (Fig. 6a). The modeled ratio was also large because  
9 approximately 80% of the  $nss-SO_4^{2-}$  was mixed with submicron particles, such as ATK, ACM  
10 and AGR (Fig. 6b). The modeled median was 0.66, which was smaller than that observed,  
11 indicating that the modeled size distribution of  $nss-SO_4^{2-}$  may have been larger than that  
12 observed or may indicate that the proportions mixed with larger COR particles might have  
13 been overestimated. The features of the  $NH_4^+$  ratio were similar to those for  $nss-SO_4^{2-}$  because  
14  $nss-SO_4^{2-}$  is a major counterpart of  $NH_4^+$ . A range of 20-60% of  $T-NH_4^+$  existed in the gas  
15 phase in summer as  $NH_3$  because the temperature was high enough for  $NH_4NO_3$  to evaporate  
16 and/or the amount of  $nss-SO_4^{2-}$  was not enough to consume  $NH_3$  gas to fix it to the aerosol  
17 phase as ammonium sulfate. Because the modeled  $nss-SO_4^{2-}$  and  $NH_4^+$  were both  
18 underestimated, the improvement of  $nss-SO_4^{2-}$  could also result in the improvement of  $NH_4^+$ .

19 The observed and modeled medians of the  $PM_1$  to  $T-NO_3^-$  ratios were 0.054 and 0.035,  
20 respectively, more than 1 order of magnitude smaller than those for  $nss-SO_4^{2-}$  and  $NH_4^+$  (Fig.  
21 6e). Those are about 1 order of magnitude larger than those for the sea-salt originated  
22 components  $T-Cl^-$ . It indicates that some fractions of nitrate are mixed with sea-salt particles  
23 as  $NaNO_3$ , while the other mixed with submicron particles as  $NH_4NO_3$ . It is discussed later  
24 more in detail in Sect. 3.6.3.

25 The observed and modeled medians of the  $PM_1$  to  $T-Cl^-$  ratios were one order of magnitude  
26 smaller than those for  $T-NO_3^-$ . Almost all (99.4% on average) of the aerosol phase  $Cl^-$  was  
27 mixed with COR particles. The modeled fractions of HCl gas showed a maximum in summer,  
28 with a value of 51%. Because anthropogenic HCl emission was not considered in the current  
29 settings of RAQM2, the modeled  $T-Cl^-$  are all of sea salt origin. The temperature is high and  
30 the air is photochemically active in summer, so the  $HNO_3$  gas concentration is also high.  
31  $HNO_3$  gas efficiently condensed onto sea-salt particles and expelled the  $Cl^-$  into the gas phase  
32 by the chlorine deficit reaction (Eq. 26) in summer.



1

### 2 3.6.2 Mixing type of sulfate

3 Fig. 7 illustrates spatial distribution of mean concentrations and mixing types of sulfate in  
4 lower atmosphere (<~1000m; averages in 1st to 7th vertical grids). The seasonal trends of the  
5 mixing type of nss-SO<sub>4</sub><sup>2-</sup> were interesting (Fig.6b and Fig.7). Nss-SO<sub>4</sub><sup>2-</sup> internally mixed with  
6 ATK + ACM was the greatest in summer (June to July; Figs.7c and 7d). Because the air is  
7 cleaner in summer, there are fewer surface areas of pre-existing aerosols for H<sub>2</sub>SO<sub>4</sub> gas to  
8 condense onto, and new particle formation would occur more frequently. In contrast, in cold  
9 seasons, due to the abundance of preexisting aerosols including soot, H<sub>2</sub>SO<sub>4</sub> gas was  
10 efficiently condensed onto the soot particles (AGR) (Figs.7e and 7f). However, the current  
11 analysis could not prove the plausibility of the mixing type. For this proof, the results should  
12 be evaluated in the future by comparing them with the measurements of the soot mixing state  
13 using a Volatility Tandem Differential Mobility Analyzer (VTDMA), a Single Particle Soot  
14 Photometer (SP2), or a Transmission Electron Microscope (TEM). The modeled nss-SO<sub>4</sub><sup>2-</sup>  
15 was mixed with COR from 10-40%. The crustal components in COR, such as Na<sup>+</sup> in sea-salt  
16 or Ca<sup>2+</sup> in Asian dust, could be counterparts of nss-SO<sub>4</sub><sup>2-</sup>. The proportions show maxima in  
17 spring from March to May (40% in April as a maximum), which coincides with the Asian  
18 dust transport period at Hedo (Fig. 5j). In the current setting of RAQM2, unfortunately, the  
19 dust particles are categorized as COR together with sea salt particles, so we cannot evaluate  
20 nss-SO<sub>4</sub><sup>2-</sup> mixed solely with Asian dust. Because the modeled nss-SO<sub>4</sub><sup>2-</sup> was mixed with COR,  
21 either with sea salt or Asian dust throughout the year, the modeled PM<sub>1</sub> to bulk ratio was  
22 approximately 0.6. The observed ratio also sometimes dropped to the modeled levels, even  
23 less than half in May. Although certain discrepancies remained between the modeled and  
24 observed ratios, the modeled partitioning may not be so far from reality.

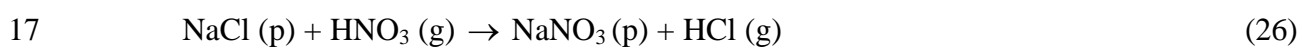
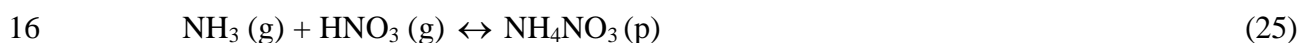
25

### 26 3.6.3 Mixing type of nitrate

27 Fig. 8 shows spatial distribution of mean concentrations and mixing types of nitrate in the  
28 lower atmosphere. The mixing type of NO<sub>3</sub><sup>-</sup> at Hedo (Fig. 6f) was interesting when it was  
29 compared with that at Gosan, Jeju Island, Korea (shown in Fig. 1 as an arrow). The observed  
30 and modeled medians of the PM<sub>1</sub> to T-NO<sub>3</sub><sup>-</sup> ratios were 0.054 and 0.035, respectively, more  
31 than 1 order of magnitude smaller than those for nss-SO<sub>4</sub><sup>2-</sup> and NH<sub>4</sub><sup>+</sup> and 1 order of

1 magnitude larger than those for Cl<sup>-</sup>. This result means that the observed and modeled T-NO<sub>3</sub><sup>-</sup>  
2 partitioned into the gas phase or internally mixed with aerosols larger than PM<sub>1</sub> were close to  
3 each other, at 94.6% and 96.5%, respectively. Kajino and Kondo (2011) made a similar  
4 analysis for the case of the PM<sub>2.5</sub>/PM<sub>10</sub> ratios of chemical components at Gosan. They  
5 calculated that 53.7% of the modeled NO<sub>3</sub><sup>-</sup> was internally mixed with sea salt particles on  
6 average in March 2005. The value was consistent with the observation, where the mean  
7 values of the modeled and observed PM<sub>2.5</sub>/PM<sub>10</sub> ratios of NO<sub>3</sub><sup>-</sup> were both 0.66. In the current  
8 simulation, 98% of the NO<sub>3</sub><sup>-</sup> was internally mixed with COR at the annual average at Hedo  
9 (Fig. 6f). The values of Fig. 8g is larger than those of Fig. 6l of Kajino and Kondo (2011)  
10 because the current figure is the average of surface to 1000 m height, while their paper  
11 showed those of surface concentration, which contains more proportion of fresh sea-salt  
12 particles. There are clear gradient in Fig. 8g from the upstream near the continent (~50%)  
13 toward downwind over the ocean (>90%).

14 The difference of the mixing type of NO<sub>3</sub><sup>-</sup> at Gosan and Hedo was explained using the  
15 following equations:



18 Gosan is located approximately 700 km upwind of Hedo, toward the Asian continent. During  
19 long-range transport, HNO<sub>3</sub> gas is produced via the photochemical oxidation of NO<sub>x</sub>. The  
20 mass transfer coefficients for each aerosol mode of category were nearly proportional to their  
21 total surface area for atmospheric aerosol size ranges (near the continuum regime). Over the  
22 continent, more than 90% of the NO<sub>3</sub><sup>-</sup> was mixed with submicron particles as NH<sub>4</sub>NO<sub>3</sub> (Eq.  
23 25; see NUC+AGR in Figs. 6j and 6k of Kajino and Kondo, 2011). We combined dust, sea-  
24 salt and anthropogenic PM<sub>10</sub> particles together as the COR category, there are substantial  
25 proportions of nitrate mixed with COR over the continent in Fig.8g, but those are not sea-salt  
26 particles. In contrast to the downwind regions of the continent over the ocean, the HNO<sub>3</sub> gas  
27 produced during transport is more efficiently condensed to sea salt particles, as the  
28 proportions of the sea salt surface area become large. The reaction of Eq. (26), occurring on/in  
29 the sea salt particles, also promoted the condensation of HNO<sub>3</sub> onto sea salt forming NaNO<sub>3</sub>.  
30 Even though the HNO<sub>3</sub> gas production during transport is less significant, the reaction Eq.  
31 (26) itself may promote the evaporation of HNO<sub>3</sub> gas in Eq. (25), because it is a reversible  
32 reaction. In this case, the conversion of NO<sub>3</sub><sup>-</sup> in submicron particles to sea salt particles might

1 occur. The fractions of nitrate with COR are predominant all over the ocean (>80%) in  
2 summer (Fig. 8h), as the temperature is higher and the fraction of HNO<sub>3</sub> gas becomes larger  
3 (Eq.25), which results in the promotion of reaction Eq.26.

4 ~~Gosan is located approximately 700 km upwind of Hedo, toward the Asian continent. The~~  
5 ~~spatial distributions of the mixing types of NO<sub>3</sub><sup>-</sup> showed that more than 90% of the NO<sub>3</sub><sup>-</sup>~~  
6 ~~could be internally mixed with sea salt over further downwind regions such as Hedo, whereas~~  
7 ~~approximately 50% is mixed with sea salt over the Yellow Sea, where Gosan is located (Fig.~~  
8 ~~6l of Kajino and Kondo, 2011).~~

9 The mixing type of NO<sub>3</sub><sup>-</sup> may be important for the size distribution of aerosols and its light  
10 scattering property. Although the same amounts of aerosol NO<sub>3</sub><sup>-</sup> existed in the air, HNO<sub>3</sub>  
11 condensed onto submicron particles forming NH<sub>4</sub>NO<sub>3</sub>, together with its water uptake,  
12 enhances the particle size efficiently and alter the light scattering property. However, HNO<sub>3</sub>  
13 condensed onto sea salt particles may not alter the particle size and optical property as  
14 significantly. It is because it expels HCl at the same time, the water uptake property may not  
15 change much, and the size increase ratio will be smaller than that for submicron particles as  
16 the sea salt particles are much larger.

### 17 3.6.4 Mixing type of soot aggregate and soot-coarse mode particle mixtures

18 Even though the simulated mixing state of soot and soot-COR mixtures were not evaluated by  
19 the measurements, we showed some examples as those are important for aerosol-radiation-  
20 cloud interaction aspects. Fig.9 illustrates mean black carbon (BC) concentration in AGR,  
21 total dry mass to BC mass ratio, and total wet mass to BC mass ratio. The SP2 measured  
22 shell/core diameter ratio in Asian continental outflow was about 1.6 (Shiraiwa et al., 2008) so  
23 the mass ratio could be around 4. Our simulated values could be significantly overestimated  
24 about 5-10 over the continent to 15-20 over the ocean (Figs 9c and 9d). The hygroscopic  
25 components mixed with AGR were simulated to uptake water about 3-4 times the original dry  
26 mass.

27 Fig.10 shows the mean number concentrations of soot aggregate (AGR), coarse mode  
28 particles (COR) and number of AGR collided to COR particles ( $M_0^{AGR}$  in Table 2). As  
29 discussed in Sect. 2.2.4,  $M_0^{AGR}$  does not mean the number of AGR-COR aggregate. The  
30 coalescence efficiency may not be unity and one COR particle can be attached by several  
31 AGR particles. In the simulation,  $M_0^{AGR}$  were comparable to  $M_0$  of COR particles (~1-10

1 particles/cm<sup>3</sup>), when  $M_0$  of AGR are 2-3 orders of magnitude larger (~1000 particles/cm<sup>3</sup>) and  
2 the BC mass concentrations are larger than 2-5  $\mu\text{g}/\text{m}^3$ . When the number concentration is low  
3 in summer (Fig. 10b) due to lower emission flux and larger convection and turbulent mixing,  
4 the probability of collision between AGR and COR particles could be significantly lower (Fig.  
5 10f).

6

## 7 4 Conclusions

8 A new aerosol chemical transport model, Regional Air Quality Model 2 (RAQM2), was  
9 developed to simulate Asian air quality. We implemented a simple version of a triple-moment  
10 modal aerosol dynamics model (MADMS; Kajino 2011) and achieved a completely dynamic  
11 (non-equilibrium) solution of a gas-to-particle mass transfer over a wide range of aerosol  
12 diameters, from 1 nm to super  $\mu\text{m}$ . To consider a variety of atmospheric aerosol properties,  
13 the category approach (Kajino and Kondo, 2011) is utilized. In RAQM2, aerosols are  
14 distributed into 4 categories: 1. particles in Aitken mode (ATK), 2. soot-free particles in  
15 accumulation mode (ACM), 3. soot aggregates (AGR) and 4. particles in coarse mode (COR).  
16 ~~In the current setting, aerosol size distribution in each category is characterized by a single~~  
17 ~~mode. New particle formation, condensation/evaporation, and intra/inter category~~  
18 ~~coagulations for each mode of categories are solved dynamically.~~ A regional-scale simulation  
19 ( $\Delta x = 60$  km) was performed for the entire year of 2006 covering the northeast Asian region.

20 ~~To evaluate the model performance on the major inorganic components in the air, we used~~  
21 ~~observed hourly air concentrations of  $\text{SO}_2$ ,  $\text{NO}_x$ ,  $\text{O}_3$ ,  $\text{PM}_{2.5}$ , and  $\text{PM}_{10}$ . We also used 1 or 2-~~  
22 ~~weekly air concentrations of aerosol  $\text{nss-SO}_4^{2-}$ , total (gas plus aerosol)  $(\text{T})\text{-NO}_3^-$ ,  $(\text{T})\text{-Cl}^-$ ,  $(\text{T})$ -~~  
23  ~~$\text{NH}_4^+$ ,  $\text{Na}^+$ , and  $\text{nss-Ca}^{2+}$  of the Acid Deposition Monitoring Network in East Asia (EANET).~~  
24 ~~Higher temporal resolution data of aerosol components were used, and the hourly~~  
25 ~~concentrations of  $\text{PM}_1\text{-nss-SO}_4^{2-}$ ,  $\text{PM}_1\text{-NO}_3^-$ ,  $\text{PM}_1\text{-Cl}^-$ , and  $\text{PM}_1\text{-NH}_4^+$  were measured using a~~  
26 ~~quadrupole aerosol mass spectrometer (Aerodyne Research Inc., Q-AMS) at the Cape Hedo~~  
27 ~~Atmospheric and Aerosol Monitoring Station (CHAAMS). Statistical analyses showed that~~  
28 ~~the model reproduced the regional-scale transport and transformation of the major inorganic~~  
29 ~~anthropogenic and natural air constituents within factors of 2 to 5. The modeled size~~  
30 ~~distributions ( $\text{PM}_{2.5}/\text{PM}_{10}$  of total weight and  $\text{PM}_1/\text{bulk}$  ratios of chemical components)~~  
31 ~~agreed quantitatively with those observed at EANET and CHAAMS sites. We concluded that~~

1 our prediction of aerosol mixing types (ATK, ACM, AGR and COR) of inorganic aerosol  
2 components such as  $\text{nss-SO}_4^{2-}$ ,  $\text{NH}_4^+$ ,  $\text{NO}_3^-$ , and  $\text{Cl}^-$  were **consistent with those in nature**.

3 The modeled mixing types of the chemical components were found to be interesting. The  
4  $\text{Nss-SO}_4^{2-}$  internally mixed with ATK + ACM was greatest in summer (June to July). Because  
5 the air is cleaner in summer, there are less surface areas of preexisting aerosols for  $\text{H}_2\text{SO}_4$  gas  
6 to condense onto; thus, new particle formation would occur more frequently. In contrast, in  
7 cold seasons, due to the abundance of pre-existing aerosols including soot,  $\text{H}_2\text{SO}_4$  gas was  
8 efficiently condensed onto the soot particles (AGR). To evaluate the results, the modeled  
9 mixing type should be evaluated in the future by comparing it with measurements of the soot  
10 mixing state using Volatility Tandem Differential Mobility Analyzer (VTDMA), Single  
11 Particle Soot Photometer (SP2), or Transmission Electron Microscope (TEM) analysis. **The**  
12 **simulated total dry mass to black carbon (BC) mass ratio was about 5-10 over the continent**  
13 **and 15-20 over the ocean, which are significantly larger than the previous measurement in**  
14 **Asian continental outflow (~4). Further efforts will be necessary to obtain the consistent**  
15 **features of Asian aerosol properties. The number of AGR collided to COR, was also**  
16 **simulated in this study, which could be comparable to the number concentration of COR (~1-**  
17 **10 particles/cm<sup>3</sup>), when the number concentrations of AGR were 2-3 orders of magnitude**  
18 **larger (~1000 particles/cm<sup>3</sup>) in cold seasons. When the concentrations of AGR were low in**  
19 **summer, the probability of collision between AGR and COR particles could be significantly**  
20 **lower.**

21 The difference in mixing type of the  $\text{NO}_3^-$  at Hedo and Gosan was interesting. Ninety-eight  
22 percent of the modeled  $\text{NO}_3^-$  was internally mixed with COR at Hedo, whereas 53.7% of the  
23  $\text{NO}_3^-$  was internally mixed with sea salt particles at Gosan (Kajino and Kondo, 2011). The  
24 modeled values were consistent with the observed  $\text{PM}_{2.5}/\text{PM}_{10}$  ratio of the  $\text{NO}_3^-$  at Gosan and  
25 the  $\text{PM}_1/\text{T-NO}_3^-$  ratio at Hedo. Gosan is located upwind of Hedo toward the Asian continent.  
26 To the downwind regions of the continent over the ocean, the  $\text{HNO}_3$  gas produced during  
27 transport is more efficiently condensed onto sea salt particles, as the proportions of the sea  
28 salt surface area to the total aerosol surface area become large. The chlorine deficit reaction  
29 on the sea salt particles promoted the condensation of  $\text{HNO}_3$ . This reaction decreases  $\text{HNO}_3$   
30 gas concentration, resulting in evaporation of  $\text{NH}_4\text{NO}_3$  from submicron particles. This  
31 conversion of nitrate in submicron particles to sea salt particles might occur during transport.

1 The aerosol mixing type is a key parameter for the light-scattering and absorbing properties,  
2 in addition to number, size, and chemistry. Further investigation is needed by comparing the  
3 results with aerosol optical thickness (AOT) or single scattering albedo (SSA) observations  
4 for the accurate assessment of aerosol-radiation interaction processes. It is also an essential  
5 parameter for predicting CCN and IN activities of aerosols. For the better understanding of  
6 the importance of those parameters in the whole aerosol–cloud–radiation interaction systems,  
7 online coupling of meteorology – chemistry models is indispensable in the near future.

8 The current model is computationally efficient in a sense that even though we consider the  
9 mixing types we need only a few numbers of transport variables as we used a modal approach,  
10 which is less accurate compared to a sectional approach. It is also efficient in aerosol process  
11 modeling because even though we used 1 s of time step to resolve the simultaneous  
12 nucleation, condensation, and coagulation processes of nano-particles, we adopted a larger  
13 time step to solve multi-component thermodynamic equilibrium state, which is  
14 computationally expensive. One box simulations with sensitivity runs (operator splitting, time  
15 splitting, number of modes or categories, or modal v.s. sectional approaches) will be useful to  
16 optimize the current method in terms of accuracy and efficiency.

## 18 **Acknowledgements**

19 This research was promoted by the Fundamental Research Budget of the Meteorological  
20 Research Institute of Japan, “Studies on Atmospheric Aerosol Properties and Processes”. The  
21 study was partly supported by the Environment Research and Technology Development Fund  
22 (Project No. B-0905 and A-1101) of the Ministry of the Environment of Japan and the  
23 Ministry of Education, Science, Sports and Culture (MEXT) Grant-in-Aid for Scientific  
24 Research (B), 23310018, 2011.

## 26 **References**

- 27 Abdul-Razzak, H., Ghan, S. J.: A parameterization of aerosol activation. 2. Multiple aerosol  
28 types, *J. Geophys. Res.*, 105(D5), 6837-6844, 2000.
- 29 An, J., Ueda, H., Wang, Z., Matsuda, K., Kajino, M., Cheng, X.: Simulations of monthly  
30 mean nitrate concentrations in precipitation. *Atmos. Environ.*, 36, 4159-4171, 2002.

1 An, J., Ueda, H., Matsuda, K. Hasome, H., and Iwata, M.: Simulated impacts of SO<sub>2</sub>  
2 emissions from the Miyake volcano on concentration and deposition of sulfur oxides in  
3 September and October of 2000. *Atmos. Environ.*, 37, 3039-3046, 2003.

4 Binkowski, F. S., Shankar, U.: The regional particulate model: 1. Model description and  
5 preliminary results, *J. Geophys. Res.*, 100, 26,191-26.209, doi:10.1029/95JD02093, 1995.

6 Byun, D., Schere, K. L.: Review of the governing equations, computational algorithms, and  
7 other components of the Models-3 Community Multiscale Air Quality (CMAQ) Modeling  
8 System, *Applied Mechanics Reviews*, 59, 51-77, 2006.

9 Carter, W.: Documentation of the SAPRC-99 chemical mechanism for VOC reactivity  
10 assessment. Final report to California Air Resources Board, Rep. 92-329, Univ. of Calif.,  
11 Riverside, 8 May., 2000.

12 Carlton, A. G., Turpin, B. J., Altieri, K. E., Seitzinger, S., Reff, A., Lim, H. -J., Ervens, B.:  
13 Atmospheric oxalic acid and SOA production from glyoxal: Results of aqueous  
14 photooxidation experiment. *Atmos. Environ.*, 41, 2007.

15 Carmichael, G. R., Sakurai, T., Streets, D., Hozumi, Y., Ueda, H., Park, S. U., Fung, C., Han,  
16 Z., Kajino, M., Engardt, M., Bannet, C., Hayami, H., Sartelet, K., Holloway, T., Wang, Z.,  
17 Kannari, A., Fu, J., Matsuda, K., Thongboonchoo, N., Amann, M.: MICS-Asia II: the model  
18 intercomparison study for Asia phase II methodology and overview of findings, *Atmos.*  
19 *Environ.*, 42, 3468-3490, 2008.

20 Chen, F., Dudhia, J.: Coupling an advanced land-surface/ hydrology model with the Penn  
21 State/ NCAR MM5 modeling system. Part I: Model description and implementation. *Mon.*  
22 *Weather Rev.*, 129, 569-585, 2001.

23 Clarke, A. D., Shinozuka, Y., Kapustin, V. N., Howell, S., Huebert, B., Doherty, S., Anderson,  
24 T., Covert, D., Anderson, J., Hua, X., Moore II, K. G., McNaughton, C., Carmichael, G. R.,  
25 Weber, R.: Size distributions and mixtures of dust and black carbon aerosol in Asian outflow:  
26 Physicochemistry and optical properties. *J. Geophys. Res.*, 109, doi:10.1029/2003JD004378,  
27 2004.

28 Clarke, A. D., Owens, S. R., Zhou, J.: An ultrafine sea-salt flux from breaking waves:  
29 Implications for cloud condensation nuclei in the remote marine atmosphere. *J. Geophys. Res.*,  
30 111, D06202, doi:10.1029/2005JD006565, 2006.

1 Deushi, M., Shibata, K.: Development of an MRI Chemistry-Climate Model ver.2 for the  
2 study of tropospheric and stratospheric chemistry, *Papers in Meteor. Geophys.*, 62, 1-46, 2011.

3 DOE, 1994: Handbook of methods for the analysis of the various parameters of the carbon  
4 dioxide system in sea water. Version 2, A. G. Dickson and C. Goyet, eds., ORNL/CDIAC-74,  
5 1994.

6 Dudhia, J.: Numerical study of convection observed during the winter monsoon experiment  
7 using a mesoscale two-dimensional model. *J. Atmos. Sci.*, 46, 3077-3107, 1989.

8 Edney, E. O., Kleindienst, T. E., Lewandowski, M., Offenberg, J. H.: Updated SOA chemical  
9 mechanism for the Community Multiscale Air Quality model. EPA 600/X-07/025, U. S.  
10 Environ. Prot. Agency, Durham, N. C., 2007.

11 Foley, K. M., Roselle, S. J., Appel, K. W., Bhave, P. V., Pleim, J. E., Otte, T. L., Mathur, R.,  
12 Sarwar, G., Young, J. O., Gilliam, R. C., Nolte, C. G., Kelly, J. T., Gilliland, A. B., Bash, J.  
13 O.: Incremental testing of the Community Multiscale Air Quality (CMAQ) modeling system  
14 version 4.7, *Geosci. Model Dev.*, 3, 205-226, 2010.

15 Fountoukis, C., Nenes, A.: ISORROPIA II: a computationally efficient thermodynamic  
16 equilibrium model for  $K^+$ - $Ca^{2+}$ - $Mg^{2+}$ - $NH_4^+$ - $Na^+$ - $SO_4^{2-}$ - $NO_3^-$ - $Cl^-$ - $H_2O$  aerosols, *Atmos. Chem.*  
17 *Phys.*, 7, 4639-4659, 2007.

18 Fuchs, N.A.: *The Mechanics of Aerosols*, Pergamon Press, Oxford, 1964.

19 Giglio, L., Randerson, J. T., van der Werf, G. R., Kasibhatla, P. S., Collatz, G. J., Morton, D.  
20 C., Defries, R. S.: Assessing variability and long-term trends in burned area by merging  
21 multiple satellite fire products. *Biogeosciences*, 7, 1171-1186, 2010.

22 Grell, G. A., Devenyi, D.: A generalized approach to parameterizing convection combining  
23 ensemble and data assimilation techniques. *Geophys. Res. Lett.* 20(14), 1693,  
24 doi:10.1029/2002GL015311, 2002.

25 Guazzotti, S. A., Coffee, K. R., Prather, K. A.: Continuous measurements of size-resolved  
26 particle chemistry during INDOEX-Intensive Field Phase 99. *J. Geophys. Res.*, 106, 28,607-  
27 28,628, 2001.

28 Guenther, A., Karl, T., Harley, P., Wiedinmyer, C., Palmer, P. I., Geron, C.: Estimates of  
29 global terrestrial isoprene emissions using MEGAN (Model of Emissions of Gases and  
30 Aerosols from Nature). *Atmos. Chem. Phys.*, 6, 3181-3210, 2006.



1 Han, Z., Ueda, H., Matsuda, K., Zhang, R., Arao, K., Kanai, Y., Hasome, H.: Model study on  
2 particle size segregation and deposition during Asian dust events in March 2002. *Journal of*  
3 *Geophysical Research* 109, D19205, doi:10.1029/2004JD004920, 2004.

4 Han, Z., Ueda, H., Matsuda, K.: Model study of the impact of biogenic emission on regional  
5 ozone and effectiveness of emission reduction scenarios over eastern China, *Tellus B*, 53,  
6 171-191, 2005.

7 Han, Z., Ueda, H., Sakurai, T.: Model study on acidifying wet deposition in East Asia during  
8 wintertime, *Atmos. Environ.*, 40, 2360-2373, 2006.

9 Han, Z.: A regional air quality model: evaluation and simulation of O<sub>3</sub> and relevant gaseous  
10 species in East Asia during spring 2001, *Environ., Modell., Softw.*, 22, 1328-1336, 2007.

11 Hirsikko, A., Nieminen, T., Gagne, S., Lehtipalo, K., Manninen, H. E., Ehn, M., Hörrak, U.,  
12 Kerminen, V.-M., Laakso, L., McMurry, P. H., Mirme, A., Mirme, S., Petäjä, T., Tammet, H.,  
13 Vakkari, V., Vana, M., Kulamala, M.: Atmospheric ions and nucleation: a review of  
14 observations. *Atmos. Chem. Phys.*, 11, 767-798, 2011.

15 Hong, S. -Y., Lin, J. -O. J.: The WRF single-moment 6-class microphysics scheme (WSM6),  
16 *J. Korean Meteor. Soc.* 42, 129-151, 2006.

17 Ishikawa, H.: Mass-consistent wind model as a meteorological preprocessor for tracer  
18 transport models, *J. Appl. Meteorol.*, 33, 733-743, 1994.

19 Jacobson, M. Z., Ginnebaugh, D. L.: Global-through-urban nested three-dimensional  
20 simulation of air pollution with a 13,600-reaction photochemical mechanism. *J. Geophys.*  
21 *Res.*, 115, D14304, doi:10.1029/2009JD013289, 2010.

22 Janjic, Z. I.: Nonsingular implementation of the Mellor-Yamada level 2.5 scheme in the  
23 NCEP Medo model, Off. Note, 437, 61 pp., Natl. Cent. for Environ. Predict., Camp Springs,  
24 Md.

25 Kajino, M., Ueda, H., Satsumabayashi, H., An, J.: Impacts of the eruption of Miyakejima  
26 Volcano on air quality over far east Asia, *J. Geophys. Res.*, 109, D21204,  
27 doi:10.1029/2004JD004762, 2004.

28 Kajino, M., Ueda, H., Satsumabayashi, H., Han, Z.: Increase in nitrate and chloride deposition  
29 in east Asia due to increased sulfate associated with the eruption of Miyakejima Volcano, *J.*  
30 *Geophys. Res.*, 110, D18203, doi:10.1029/2005JD005879, 2005.

- 1 Kajino, M., Ueda, H., Nakayama, S.: Secondary acidification: Changes in gas-aerosol  
2 partitioning of semivolatile nitric acid and enhancement of its deposition due to increased  
3 emission and concentration of SO<sub>x</sub>. *J. Geophys. Res.*, 113, D03302,  
4 doi:10.1029/2007JD008635, 2008.
- 5 Kajino, M.: MADMS: Modal Aerosol Dynamics model for multiple Modes and fractal  
6 Shapes in the free-molecular and near-continuum regimes. *J. Aerosol Sci.*, 42, 224-248, 2011.
- 7 Kajino, M., Kondo, Y.: EMTACS: Development and regional-scale simulation of a size,  
8 chemical, mixing type, and soot shape resolved atmospheric particle model. *J. Geophys. Res.*,  
9 116, D02303, doi:10.1029/2010JD015030, 2011.
- 10 Kang, J.-Y., Yoon, S.-C., Shao, Y., Kim, S.-W.: Comparison of vertical dust flux by  
11 implementing three dust emission schemes in WRF/Chem., *J. Geophys. Res.*, 116, D09202,  
12 doi:10.1029/2010JD014649, 2011.
- 13 Katata, G., Nagai, H., Wrzesinsky, T., Klemm, O., Eugster, W., Burkard, R.: Development of  
14 a land surface model including cloud water deposition on vegetation, *J. Appl. Meteor.*  
15 *Climatol.*, 47, 2129-2146, 2008.
- 16 Katata, G., Nagai, H., Zhang, L., Held, A., Serça, D., Klemm, O.: Development of an  
17 atmosphere-soil-vegetation model for investigation of radioactive materials transport in the  
18 terrestrial biosphere, *Prog. Nucl. Sci. Technol.*, 2, 530-537, 2011 (online available:  
19 <http://www.aesj.or.jp/publication/pnst002/data/530-537.pdf>).
- 20 Kirsch, A.A., Fuchs, N.A.: Studies on fibrous aerosol filters. III . Diffusional deposition of  
21 aerosols in fibrous filters, *Ann. Occup. Hyg.*, 11, 299-304, 1968.
- 22 Kuang, C., McMurry, P. H., McCormick, A. V., Eisele, F. L.: Dependence of nucleation rates  
23 on sulfuric acid vapor concentration in diverse atmospheric locations. *J. Geophys. Res.* 113,  
24 D10209, doi:10.1029/2007JD009253, 2008.
- 25 Kulmala, M., Kerminen, V.-M.: On the formation and growth of atmospheric nanoparticles.  
26 *Atmos. Res.*, 90, 132-150, 2008.
- 27 Kurokawa, J., Ohara, T., Uno, I., Hayasaka, M., Tanimoto, H.: Influence of meteorological  
28 variability on interannual variations of springtime boundary layer ozone over Japan during  
29 1981-2005. *Atmos. Chem. Phys.*, 9, 6287-6304, 2009.

1 Lin, Y. -L., Farley, R. D., Orville, H. D.: Bulk parameterization of the snow field in a cloud  
2 model. *J. Clim. Appl. Meteorol.*, 22, 1065-1092, 1983.

3 Lohmann, U., Diehl, K.: Sensitivity studies of the importance of dust ice nuclei for the  
4 indirect aerosol effect on stratiform mixed-phase clouds. *J. Atmos. Sci.*, 63, 968-982, 2010.

5 Madronich, S.: Photodissociation in the atmosphere: 1. Actinic flux and the effects of ground  
6 reflections and clouds. *J. Geophys. Res.*, 92, 9740-9752, doi:10.1029/JD092iD08p09740,  
7 1987.

8 Mlawer, E. J., Taubman, S. J., Brown, P. D., Iacono, M. J., Clough, S. A.: Radiative transfer  
9 for inhomogeneous atmosphere, RRTM, a validated correlated-k model for the long wave, *J.*  
10 *Geophys. Res.*, 102, 16,663-16,682, doi:10.1029/97JD00237, 1997.

11 Myneni, R. B., Hoffman, S., Knyazikhin, Y., Privette, J. L., Glassy, J., Tian, Y., Wang, Y.,  
12 Song, X., Zhang, Y., Smith, G. R., Lotsch, A., Friedl, M., Morisette, J. T., Votava, P., Nemani,  
13 R. R., Running S. W.: Global products of vegetation leaf area and fraction absorbed PAR  
14 from year one of MODIS data. *Remote Sensing of Environment*, 83, 214-231, 2002.

15 Nagashima, T., Ohara, T., Sudo, K., Akimoto, H.: The relative importance of various source  
16 regions on East Asian surface ozone. *Atmos. Chem. Phys.*, 10, 11,305-11,322, 2010.

17 Ohara, T., Akimoto, H., Kurokawa, J., Horii, N., Yamaji, K., Yan, X., Hayasaka, T.: An  
18 Asian emission inventory of anthropogenic emission sources for the period 1980-2020. *Atmos.*  
19 *Chem. Phys.*, 7, 4419-4444, 2007.

20 Peters, K., Eiden, R.: Modelling the dry deposition velocity of aerosol particles to a spruce  
21 forest, *Atmos. Environ.*, 26A, 2555-2564, 1992.

22 Petroff, A., Zhang, L.: Development and validation of a size-resolved particle dry deposition  
23 scheme for application in aerosol transport models, *Geosci. Model Dev.*, 3, 753-769, 2010.

24 Pleim, J. E., Chang, J. S.: A non-local closure model for vertical mixing in the convective  
25 boundary layer. *Atmos. Environ.*, 26A, 965-981, 1992.

26 Pruppacher, H. R., Klett, J. D.: *Microphysics of Clouds and Precipitation*, Kluwer Acad.,  
27 Norwell, Mass., 1997.

28 Sekiyama, T. T., Tanaka, T. Y., Shimizu, A., Miyoshi, T.: Data assimilation of CALIPSO  
29 aerosol observations., *Atmos. Chem. Phys.* 10, 39-49, 2010.

1 Shiraiwa, M., Kondo, Y., Moteki, N., Takegawa, N., Sahu, L. K., Takami, A., Hatakeyama, S.,  
2 Yonemura, S., Blake, D. R.: Radiative impact of mixing state of black carbon aerosol in Asian  
3 outflow, *J. Geophys. Res.*, 11, D24210, doi:10.1029/2008JD010546, 2008.

4 Skamarock, W. C., Klemp, J. B., Dudhia, J., Gill, D. O., Barker, D. M., Duda, M. G., Huang,  
5 X. Y., Wang, W., Powers, J. G.: A description of the advanced research WRF version 3, Tech.  
6 Note, NCAR/TN~475+STR, 125 pp., Natl. Cent. for Atmos. Res., Boulder, Colo., 2008.

7 Song C. H., Carmichael, G. R.: A 3D modeling investigation of the evolution processes of  
8 dust and sea-salt particles in east Asia. *J. Geophys. Res.*, 106(D16) 18,131 – 18,154, 2001.

9 Sudo, K., Akimoto, H.: Global source attribution of tropospheric ozone: Long-range transport  
10 from various source regions. *J. Geophys. Res.*, 112, D12302, doi:10.1029/2006JD007992,  
11 2007.

12 Takami, A., Miyoshi, T., Shimono, A., Kaneyasu, N., Kato, S., Kajii, Y., and Hatakeyama, S.:  
13 Transport of anthropogenic aerosols from Asia and subsequent chemical transformation. *J.*  
14 *Geophys. Res.*, 112, D22S31, doi:10.1029/2006JD008120, 2007.

15 Takiguchi, Y., Takami, A., Sadanaga, Y., Lun, X., Shimizu, A., Matsui, I., Sugimoto, N.,  
16 Wang, W., Bandow, H., and Hatakeyama, S.: Transport and transformation of total reactive  
17 nitrogen over the East China Sea. *J. Geophys. Res.*, 113, D10306, doi:10.1029/2007JD009462,  
18 2008.

19 Walcek, C. J., Aleksic, N. M.: A simple but accurate mass conservative peak-preserving,  
20 mixing ratio bounded advection algorithm with fortran code. *Atmos. Environ.*, 32, 3863-3880,  
21 1998.

22 Walcek, C. J., Taylor, G. R.: A theoretical method for computing vertical distributions of  
23 acidity and sulfate production within cumulus clouds. *J. Atmos. Sci.*, 43, 339-355, 1986.

24 Wang, Z., Akimoto, H., Uno, I.: Neutralization of soil aerosol and its impact on the  
25 distribution of acid rain over east Asia: Observations and model results, *J. Geophys. Res.*, 107,  
26 D19, 4389, doi:10.1029/2001JD001040, 2002.

27 Whitby, E. R., McMurry, P. H.: Modal aerosol dynamics modeling, *Aerosol Sci. Technol.*, 27,  
28 673-688, 1997.

1 Yang, W., Shabanov, N. V., Huang, D., Wang, W., Dickinson, R. E., Nemani, R.R.,  
2 Knyazikhin, Y., Myneni, R. B.: Analysis of leaf area index products from combination of  
3 MODIS Terra and Aqua data, *Remote Sensing of Environment*, 104, 297-312, 2006.

4 Yumimoto, K., Uno, I., Sugimoto, N., Shimizu, A., Liu, Z., Winker, D.M.: Adjoint inversion  
5 modeling of Asian dust emission using lidar observations, *Atmos. Chem. Phys.* 8, 2869-2884,  
6 2008.

7 Zhang, L., Gong, S., Padro, J., Barrie, L.: A size-segregated particle dry deposition scheme  
8 for an atmospheric aerosol module. *Atmos. Environ.*, 35, 549-560, 2001.

9 Zhang, L., Brook, J. R., Vet, R.: A revised parameterization for gaseous dry deposition in air-  
10 quality models. *Atmos. Chem. Phys.*, 3, 2067-2082, 2003.

11 Zhang, Q., Streets, D. G., Carmichael, G. R., He, K. B., Huo, H., Kannari, A., Klimont, Z.,  
12 Park, L. S., Reddy S., Fu, J. S., Chen, D., Duan, L., Lei, Y., Wang, L. T., Yao, Z. L.: Asian  
13 emission in 2006 for the NASA INTEX-B mission. *Atmos. Chem. Phys.*, 9, 5131-5133, 2009.

14 Zhang, Y., McMurry, P. H., Yu, F., Jacobson, M. Z.: A comparative study of nucleation  
15 parameterizations: 1. Examination and evaluation of the formulations. *J. Geophys. Res.*, 115,  
16 D20212, doi:10.1029/2010JD014150, 2010.

17 Zhu, A., Ramanathan, V., Li, F., Kim, D.: Dust plumes over the Pacific, Indian and Atlantic  
18 Oceans: Climatology and radiative impact. *J. Geophys. Res.*, 112, doi:10.1029/2007JD008427,  
19 2007.

20  
21

1 **Table 1.** List of data and schemes used in the WRF and RAQM2 models

Scheme	Name / reference
<i>WRF</i>	
Initial and boundary conditions, analysis nudging	National Center for Environmental Prediction (NCEP) final operational global analysis data (available from <a href="http://dss.ucar.edu/datasets/ds083.2">http://dss.ucar.edu/datasets/ds083.2</a> )
Planetary boundary layer	Mellor-Yamada-Janjic (MYJ) model (Janjic, 2002)
Grid-scale cloud microphysics parameterization	The six-class scheme WSM6 (Lin et al, 1983)
Subgrid-scale cumulus parameterization	Grell and Devenyi (2002)
Land surface model	Noah LSM (Chen and Dudhia, 2001)
Long-wave radiation	RRTM (Mlawer et al., 1997)
Short-wave radiation	Dudhia (1989)
<i>RAQM2</i>	
Boundary condition of O <sub>3</sub> and its precursors	MRI-CCM2 (Deushi and Shibata, 2011) climatological value
Emission (anthropogenic, biogenic, open biomass burning, mineral dust, sea-salt)	REAS (Ohara et al., 2007; Kurokawa et al., 2009), GFED3(Giglio et al., 2010), MEGAN2 (Guenther et al., 2006), Asian dust (Han et al., 2004), Sea-salt (Clarke et al., 2006)
Advection	MPMAA (Walcek and Aleksic, 1998)
J-value	Madronich (1987) with TOMS O <sub>3</sub> column data (available from <a href="ftp://toms.gsfc.nasa.gov">ftp://toms.gsfc.nasa.gov</a> )
Gas chemistry	72 species and 214 reactions (SAPRC99; Carter, 2000)
SOA chemistry	Edney et al. (2007)
Liquid chemistry	Walcek and Taylor (1986); Carlton et al. (2007)
New particle formation	Kuang et al. (2008)
Aerosol dynamics (condensation, evaporation, coagulation)	This study and MADMS (Kajino, 2011)
Surface gas-aerosol equilibrium of inorganic and organic compounds	ISORROPIA2 (Fountoukis and Nenes, 2007), Edney et al. (2007)
Dry deposition	This study and Zhang et al. (2001), (2003), Katata et al. (2008), (2011)
CCN activation	Abdul-Razzak and Ghan (2000)
IN activation	Lohmann and Diehl (2010)
Grid-scale cloud microphysics	Lin et al. (1983)
Collision of aerosol to grid-scale rain, snow and graupel droplets	This study
Sub-grid-scale convection and wet deposition	ACM (Pleim and Chang, 1992)

1 **Table 2.** Aerosol categories and **transported variables** in the RAQM2 model

Category number	Category name	Physical components		Chemical compositions										
		$M_0$	$M_2$											
1	ATK	$M_0$	$M_2$	-	-	-	-	-	-	$\text{SO}_4^{2-}$	$\text{NH}_4^+$	$\text{NO}_3^-$	$\text{Cl}^-$	$\text{H}_2\text{O}$
2	ACM	$M_0$	$M_2$	UID	-	OA	-	-	-	$\text{SO}_4^{2-}$	$\text{NH}_4^+$	$\text{NO}_3^-$	$\text{Cl}^-$	$\text{H}_2\text{O}$
3	AGR	$M_0$	$M_2$	UID	BC	OA	-	-	-	$\text{SO}_4^{2-}$	$\text{NH}_4^+$	$\text{NO}_3^-$	$\text{Cl}^-$	$\text{H}_2\text{O}$
4	COR	$M_0$	$M_2$	UID	BC	OA	DU	SS	-	$\text{SO}_4^{2-}$	$\text{NH}_4^+$	$\text{NO}_3^-$	$\text{Cl}^-$	$\text{H}_2\text{O}$
		$M_0^{AGR}$												

2

3 **Table 3.** Rules for transfer of the three moments and chemical mass concentrations from one  
4 category to another due to inter-category coagulation and mode merging

Rule Number	Rule
<i>Inter-category Coagulation</i>	
1	1.ATK + 2.ACM $\rightarrow$ 2.ACM
2	1.ATK + 3.AGR $\rightarrow$ 3.AGR
3	1.ATK + 4.COR $\rightarrow$ 4.COR
4	2.ACM + 3.AGR $\rightarrow$ 3.AGR
5	2.ACM + 4.COR $\rightarrow$ 4.COR
6	3.AGR + 4.COR $\rightarrow$ 4.COR
<i>Mode Merging</i>	
7	(swelling) 1.ATK $\rightarrow$ 2.ACM
8	(shrinking) 2.ACM $\rightarrow$ 1.ATK

5

6

7

- 1 **Table 4.** Description of the EANET remote sites and the CHAAMS site used in this study.
- 2 Each station is depicted in Figure 1.

	Longitude (E)	Latitude (N)	Altitude (m a.s.l.)	Character- istics	X	Y	MT	AT	AT- PM <sub>2.5</sub>	FP	AMS
1. Rishiri	141°12'	45°07'	40	Remote	68	48	1h	1h	1h	2w	N.A.
2. Tappi	140°21'	41°15'	105	Remote	69	41	1h	1h	N.A.	2w	N.A.
3. Ogasawara	142°13'	27°05'	230	Remote	77	16	1h	1h	N.A.	1w	N.A.
4. Sado	138°24'	38°14'	136	Remote	67	35	1h	1h	N.A.	2w	N.A.
5. Oki	133°11'	36°17'	90	Remote	60	30	1h	1h	1h	2w	N.A.
6. Hedo & CHAAMS	128°15'	26°52'	60	Remote	54	12	1h	1h	N.A.	2w	1h

- 3 X,Y: Model grid number; MT: meteorological parameters, AT: automatically monitored (NO<sub>x</sub>,
- 4 O<sub>3</sub>, SO<sub>2</sub>, PM<sub>10</sub>; PM<sub>2.5</sub> is only available at Rishiri and Oki), FP: filter pack method (Aerosol
- 5 inorganic components), AMS: aerosol mass spectrometer, only available at CHAAMS.
- 6 CHAAMS is located within the same premises as the EANET Hedo station. 1h: hourly, 1w:
- 7 weekly, 2w: 2 weekly.

8  
9  
10  
11  
12  
13  
14  
15  
16  
17  
18  
19  
20



1 **Table 5.** Statistical analysis for comparison between all EANET data of observation and  
 2 simulation for 2006.

	Unit	Number of data	Median (Obs.)	Median (Sim.)	RMSE	R	FAC2 <sup>a</sup>	FAC5 <sup>b</sup>
Daily mean bulk gas concentrations (AT <sup>d</sup> )								
O <sub>3</sub> <sup>c</sup>	ppbv	2093	50.3	51.2	16.9	0.47	0.96	1.00
SO <sub>2</sub>	ppbv	2052	0.17	0.25	0.70	0.52	0.36	0.64
NO <sub>x</sub>	ppbv	1819	0.80	0.58	1.1	0.49	0.52	0.86
1- or 2-weekly bulk concentrations of chemical compounds (FP <sup>e</sup> )								
Nss-SO <sub>4</sub> <sup>2-</sup>	μg m <sup>-3</sup>	152	1.9	1.3	1.9	0.70	0.46	0.80
T-NH <sub>4</sub> <sup>+</sup>	μg m <sup>-3</sup>	138	0.71	0.45	0.69	0.52	0.50	0.81
T-NO <sub>3</sub> <sup>-</sup>	μg m <sup>-3</sup>	144	0.92	1.8	2.2	0.59	0.47	0.87
T-Cl <sup>-</sup>	μg m <sup>-3</sup>	144	3.7	2.8	4.2	0.13	0.42	0.89
Na <sup>+</sup>	μg m <sup>-3</sup>	144	2.3	1.4	2.5	0.13	0.38	0.85
Nss-Ca <sup>2+</sup>	μg m <sup>-3</sup>	152	0.056	0.11	0.24	0.55	0.38	0.67
Daily mean PM <sub>2.5</sub> and PM <sub>10</sub> concentration and their ratios (AT)								
PM <sub>2.5</sub>	μg m <sup>-3</sup>	696	8.8	5.2	10.8	0.45	0.52	0.87
PM <sub>10</sub>	μg m <sup>-3</sup>	2141	17.7	8.3	19.1	0.65	0.45	0.81
PM <sub>2.5</sub> /PM <sub>10</sub>	-	674	0.57	0.49	0.26	0.018	0.83	1.00

3 a. Fraction of data that satisfy a factor of 2.

4 b. Fraction of data that satisfy a factor of 5.

5 c. Daily maximum 8 hour mean.

6 d. Measured by automatic instruments.

7 e. Measured by the filter pack method.

8

9

10

11

12

1 **Table 6.** Statistical analysis for comparison between observation and simulation at the Hedo  
 2 EANET and CHAAMS stations.

	unit	Number of data	Median (Obs.)	Median (Sim.)	RMSE	R	FAC2	FAC5
Daily PM <sub>1</sub> concentrations (AMS <sup>a</sup> )								
PM <sub>1</sub> -nss-SO <sub>4</sub> <sup>2-</sup>	μg m <sup>-3</sup>	199	4.2	1.3	4.4	0.57	0.28	0.72
PM <sub>1</sub> -NH <sub>4</sub> <sup>+</sup>	μg m <sup>-3</sup>	199	1.0	0.34	1.0	0.56	0.28	0.70
PM <sub>1</sub> -NO <sub>3</sub> <sup>-</sup>	μg m <sup>-3</sup>	199	0.088	0.080	0.15	0.30	0.53	0.90
PM <sub>1</sub> -Cl <sup>-</sup>	μg m <sup>-3</sup>	197	0.027	0.016	0.088	0.097	0.26	0.58
2-weekly bulk concentrations of chemical compounds (FP <sup>b</sup> )								
Nss-SO <sub>4</sub> <sup>2-</sup>	μg m <sup>-3</sup>	22	5.9	2.0	3.0	0.83	0.32	0.86
T-NH <sub>4</sub> <sup>+</sup>	μg m <sup>-3</sup>	20	1.4	0.47	0.91	0.56	0.20	0.80
T-NO <sub>3</sub> <sup>-</sup>	μg m <sup>-3</sup>	22	1.7	2.6	1.7	0.49	0.72	1
T-Cl <sup>-</sup>	μg m <sup>-3</sup>	22	8.2	2.8	5.6	0.35	0.22	0.86
Na <sup>+</sup>	μg m <sup>-3</sup>	22	5.1	1.6	3.6	0.30	0.22	0.86
Nss-Ca <sup>2+</sup>	μg m <sup>-3</sup>	22	0.14	0.11	0.19	0.74	0.55	0.81
2-weekly PM <sub>1</sub> to total concentration ratios (AMS/FP)								
Nss-SO <sub>4</sub> <sup>2-</sup>	-	12	0.85	0.66	0.32	-	0.92	1
T-NH <sub>4</sub> <sup>+</sup>	-	12	0.81	0.71	0.26	-	0.92	1
T-NO <sub>3</sub> <sup>-</sup>	-	12	0.054	0.035	0.027	-	0.75	1
T-Cl <sup>-</sup>	-	12	0.0038	0.0080	0.0082	-	0.33	0.67

3 a. Measured by quadrupole aerosol mass spectrometer (Aerodyne Research Inc., Q-AMS)

4 b. Measured by the filter pack method.

5

6

7

8

9

10

1 **Figure 1.** Model domain showing terrestrial elevation (m) and the six Japanese EANET sites  
2 (1. Rishiri, 2. Tappi, 3. Ogasawara, 4. Sado, 5. Oki, 6. Hedo) and the CHAAMS sites (located  
3 in the same premises as the EANET Hedo stations). The descriptions of the locations are  
4 given in Table 4. An arrow indicates the Gosan site on Jeju Island, Korea.

5

6 **Figure 2.** Schematic illustration of (a) operator splitting and time splitting for the RAQM2  
7 aerosol dynamics module and (b) changes in moments and LNSD parameters when passing  
8 each process operator.

9

10 **Figure 3.** Scatter diagram between observed and modeled concentrations of biweekly (a)-(c)  
11 nss-SO<sub>4</sub><sup>2-</sup>, (d)-(f) T-NH<sub>4</sub><sup>+</sup>, (g)-(i) T-NO<sub>3</sub><sup>-</sup>, (j)-(l) Na<sup>+</sup>, and (m)-(o) nss-Ca<sup>2+</sup> at (left) Rishiri,  
12 (center) Oki and (right) Hedo. Solid lines denote the 1:1 line, and dashed lines denote the  
13 factor of 2 envelope.

14

15 **Figure 4.** Daily mean observed (blue) and modeled (red) concentrations of (a)-(b) PM<sub>10</sub>, (c)-  
16 (d) PM<sub>2.5</sub>, (e)-(f) PM<sub>2.5</sub>/PM<sub>10</sub> concentration ratios (the median with 75 and 25 percentile  
17 values) and modeled constituent fractions of (g)-(h) PM<sub>10</sub>, (i)-(j) PM<sub>2.5</sub>, and (k)-(l) PM<sub>1</sub>  
18 concentrations at (left) Rishiri and (right) Oki. Among the constituents, ATK+ACM (red) is  
19 the total dry mass (SO<sub>4</sub><sup>2-</sup>, NH<sub>4</sub><sup>+</sup>, NO<sub>3</sub><sup>-</sup>, Cl<sup>-</sup>, UID and OA) of the ATK and ACM categories,  
20 AGR (green) is the total dry mass (UID, BC, OA, SO<sub>4</sub><sup>2-</sup>, NH<sub>4</sub><sup>+</sup>, NO<sub>3</sub><sup>-</sup>, and Cl<sup>-</sup>) of the AGR  
21 category, COR-DU (yellow) is the dust mass (DU) of the COR category, COR-SS (blue) is  
22 the sea-salt mass (SS+Cl<sup>-</sup>) in the COR category and COR-Other (sky blue) is the other  
23 components (UID, BC, OA, SO<sub>4</sub><sup>2-</sup>, NH<sub>4</sub><sup>+</sup>, and NO<sub>3</sub><sup>-</sup>) in the COR category.

24

25 **Figure 5.** (Left) daily mean AMS measured (blue, left axis) and modeled (red, right axis) PM<sub>1</sub>  
26 (a) nss-SO<sub>4</sub><sup>2-</sup>, (c) NH<sub>4</sub><sup>+</sup>, (e) NO<sub>3</sub><sup>-</sup>, and (g) Cl<sup>-</sup> concentrations at Hedo (CHAAMS). (Right)  
27 biweekly FP measured and modeled (b) nss-SO<sub>4</sub><sup>2-</sup>, (d) T-NH<sub>4</sub><sup>+</sup>, (f) T-NO<sub>3</sub><sup>-</sup>, (h) T-Cl<sup>-</sup>, (i) Na<sup>+</sup>,  
28 and (j) nss-Ca<sup>2+</sup> concentrations at Hedo (EANET).

29

1 **Figure 6.** (Left) biweekly mean  $PM_{10}$  to total (gas plus aerosol) concentration ratios and  
2 (Right) the modeled fractions of gas phase (grey), ATK+ACM category (red), AGR category  
3 (green), and COR category (blue) aerosols of (a)-(b)  $nss-SO_4^{2-}$ , (c)-(d)  $T-NH_4^+$ , (e)-(f)  $T-NO_3^-$ ,  
4 and (g)-(h)  $T-Cl^-$  at Hedo.

5

6 **Figure 7.** Spatial distributions of mean concentrations and mixing types of sulfate in lower  
7 atmosphere ( $< \sim 1000m$ ) in (left) March and (right) July. (a)-(b) sulfate concentration ( $\mu m/m^3$ ),  
8 (c)-(d) fraction of sulfate mixed with non-light-absorbing particles (ATK + ACM) (%), (e-f)  
9 fraction of sulfate mixed with light-absorbing particles (AGR) (%).

10

11 **Figure 8.** Spatial distributions of mean concentrations and mixing types of nitrate in lower  
12 atmosphere ( $< \sim 1000m$ ) in (left) March and (right) July. (a)-(b) total-nitrate (gas plus aerosol)  
13 concentration ( $\mu m/m^3$ ), (c)-(d) nitric acid gas concentration ( $\mu m/m^3$ ), (e)-(f) fraction of nitrate  
14 mixed with submicron particles (ATK + ACM + AGR) (%), (g)-(h) fraction of nitrate mixed  
15 with coarse mode particles (COR) (%).

16

17 **Figure 9.** Spatial distributions of mean concentrations and mixing types of black carbon in  
18 lower atmosphere ( $< \sim 1000m$ ) in (left) March and (right) July. (a)-(b) black carbon  
19 concentration ( $\mu m/m^3$ ), (c)-(d) dry mass to black carbon mass ratio (-), (e)-(f) wet mass to  
20 black carbon mass ratio (-).

21

22 **Figure 10.** Spatial distributions of mean number concentrations in (left) March and (right)  
23 July of (a)-(b) soot (particles/cm<sup>3</sup>), (c)-(d) coarse mode particles (dust, sea-salt, and  
24 anthropogenic  $PM_{10}$ ) (particles/cm<sup>3</sup>) and (e)-(f) number of soot aggregate collided with coarse  
25 mode particles (particles/cm<sup>3</sup>).